JM PAPERS

A diffusion-based wind turbine wake model

Karim Ali[1]**, Tim Stallard**[1] **and Pablo Ouro**[1],†

[1]School of Engineering, University of Manchester, Manchester M13 9PL, UK

Describing the evolution of a wind turbine's wake from a top-hat profile near the turbine to a Gaussian profile in the far wake is a central feature of many engineering wake models. Existing approaches, such as super-Gaussian wake models, rely on a set of tuning parameters that are typically obtained from fitting high-fidelity data. In the current study, we present a new engineering wake model that leverages the similarity between the shape of a turbine's wake normal to the streamwise direction and the diffusion of a passive scalar from a disk source. This new wake model provides an analytical expression for a streamwise scaling function that ensures the conservation of linear momentum in the wake region downstream of a turbine. The model also considers the different rates of wake expansion that are known to occur in the near- and far-wake regions. Validation is presented against high-fidelity numerical data and experimental measurements from the literature, confirming a consistent good agreement across a wide range of turbine operating conditions. A comparison is also drawn with several existing engineering wake models, indicating that the diffusion-based model consistently provides more accurate wake predictions. This new unified framework allows for extensions to more complex wake profiles by making adjustments to the diffusion equation. The derivation of the proposed model included the evaluation of analytical solutions to several mathematical integrals that can be useful for other physical applications.

Key words: wakes

1. Introduction

Wind energy has emerged as a crucial source of renewable energy, with global installed capacity surpassing 1 TW by the end of 2023 (Global Wind Energy Council 2024). With ambitions to double this capacity by 2030, optimising wind-farm efficiency and minimising energy losses due to wake effects becomes imperative. Although clustering

† Email address for correspondence: pablo.ouro@manchester.ac.uk

wind turbines can be economically advantageous, such as through shorter connections, it increases the potential for power losses due to wake interactions, underscoring the need for fast computational tools (Balakrishnan & Hur 2022). Computational models like large eddy simulation (LES) and Reynolds-averaged Navier–Stokes (RANS) provide detailed insights into turbine loading and wake physics but are computationally intensive (Tabib, Rasheed & Kvamsdal 2015; Maas & Raasch 2022). Additionally, mesoscale models are used for studying large-scale interactions within the turbulent atmospheric boundary layer, albeit with less detail in wake resolution compared with RANS and LES microscale models (Fitch *et al.* 2012; Ali *et al.* 2023).

For more rapid analysis, engineering wake models are popular in various wind-energy applications, including layout optimisation (e.g. Hou *et al.* 2016), wind-farm control (e.g. Bay *et al.* 2018; Shapiro, Starke & Gayme 2022) and farm-to-farm interactions (e.g. van der Laan *et al.* 2023; Freitas *et al.* 2024). These models often assume the wake behind a turbine is self-similar, and is defined by a streamwise deficit function and a shape function that describes the deficit distribution normal to the flow direction. Various shape functions have been proposed in the literature including a top-hat profile (Jensen 1983; Larsen 1988), a Gaussian profile (Bastankhah & Porté-Agel 2014, 2016; Ishihara & Qian 2018), a double-Gaussian profile (Keane *et al.* 2016; Schreiber, Balbaa & Bottasso 2020) and a super-Gaussian profile (Shapiro *et al.* 2019; Blondel & Cathelain 2020; Cathelain *et al.* 2020; Blondel 2023). Downstream of a wind turbine, the shape of the wake normal to the streamwise direction evolves from a uniform profile (top hat), or a double-Gaussian-like profile in the case of non-uniform disk loading, to a Gaussian profile far enough from the turbine. The ability to model this streamwise evolution is an important feature to include in a low-fidelity wake model.

In a Gaussian wake model, the distribution of the wind-speed deficit normal to the streamwise direction is assumed to be proportional to $\exp(-r^2/(2\sigma^2))$, where r is the radial distance from the wake centre, and σ is a length scale acting as the standard deviation of the Gaussian distribution (Bastankhah & Porté-Agel 2014). The assumption of a Gaussian wake shape has been shown to accurately match experimental measurements and simulation results far enough from the wake source (e.g. Pedersen *et al.* 2022), but is not applicable close to the wake source i.e. in the near wake (Krutova *et al.* 2020). A super-Gaussian wake model extends the limitations of a Gaussian wake by assuming that the wake distribution normal to the streamwise direction is proportional to $\exp(-r^n/(2\sigma^2))$, where n is a super-Gaussian exponent obtained, typically, by fitting LES results (Blondel & Cathelain 2020; Ouro & Lazennec 2021). Having a super-Gaussian exponent $n(x)$ that varies in the streamwise direction x enables modelling of the flatness in the shape of the wind-speed deficit in the near wake, while asymptotically approaching a Gaussian wake profile far from the wake source (Shapiro *et al.* 2019).

Blondel & Cathelain (2020) suggested an alternative formulation to the super-Gaussian profile compared with that of Shapiro *et al.* (2019) based on enforcing the conservation of mass and momentum, and provided an empirical form for the streamwise evolution of the super-Gaussian exponent $n(x)$ by fitting LES data. This model was later re-calibrated by Blondel (2023) by giving more weight to the far wake than the near wake when optimising the empirical constants of the model to have better agreement with LES results. A similar approach was followed by Cathelain *et al.* (2020), who suggested a different empirical form for the wake expansion, and consequently a variant expression for $n(x)$, by giving more weight to the near wake than to the far wake. Other modifications to the super-Gaussian model include extension to three dimensions (non-axisymmetric wake) for terrain effects (Zhang *et al.* 2023; Dai *et al.* 2024) and to vertical-axis wind turbines (Ouro & Lazennec 2021).

The similarity between the distribution of the wind-speed deficit normal to the streamwise direction and the diffusion of a passive scalar provides an alternative representation to the streamwise evolution of the wake shape (Göçmen *et al.* 2016). Cheng & Porté-Agel (2018) made use of this similarity and introduced a wake model based on Taylor's diffusion theory of a passive scalar in a turbulent flow (Taylor 1921; Hay & Pasquill 1959), which was extended by Vahidi & Porté-Agel (2022) to include the effect of turbine-induced turbulence. However, both models rely on estimating Lagrangian statistics of the free-stream flow by calculating Eulerian statistics of an upstream point from a high-fidelity simulation, such as LES, and making use of the scaled similarity between Lagrangian and Eulerian statistics (Hay & Pasquill 1959; Hanna 1981). Having high-fidelity data *a priori* is not suitable for many applications that rely on simulating a large number of turbine–wake interactions such as farm control and the estimation of a farm's annual energy production (Howland *et al.* 2020; Zhan, Letizia & Iungo 2020).

In this study, we build upon the premise of Cheng & Porté-Agel (2018) by developing an analytical solution to the diffusion equation of a passive scalar emitted from a circular disk source, similar to Vahidi & Porté-Agel (2022), rather than a point source situated at a virtual origin upstream of the turbine. The key in such approach is to provide an analytical form to a streamwise scaling function that ensures that the solution of the diffusion equation conserves linear momentum at all distances downstream of the turbine. The diffusion-based model accounts for the streamwise evolution of the wake profile through a physics-based principle (i.e. diffusion normal to the streamwise direction) rather than the empirical super-Gaussian exponent $n(x)$ that is not typically related to the physics of the wake. The proposed model also alleviates the need to evaluate Lagrangian statistics from high-fidelity data. Furthermore, super-Gaussian models can provide less accurate results when applied to datasets that were not included in their calibration process, as later shown in § 3. Within a unified framework, diffusion-based wake models offer a higher degree of freedom regarding the wake shape through controlling the distribution of the passive scalar across the source disk.

The rest of the paper is structured as follows. The new wake model is introduced in § 2, where the solution to the diffusion equation is discussed in § 2.1. Discussions on the conservation of linear momentum in the wake region and on far-wake expansion are presented in §§ 2.2 and 2.3, respectively. A modification to the far-wake expansion that takes into account near-wake effects is presented in § 2.4, and the size of the passive scalar disk source is discussed in § 2.5. A step-by-step summary of the proposed model is presented in § 2.6. In § 3, the proposed model is validated against published LES data and experimental measurements, and is compared with other engineering wake models from the literature. The main findings of this paper are discussed in more detail in § 4, and are summarised in § 5. Appendix A suggests a solution to the diffusion equation, and Appendix B derives an analytical solution to a streamwise scaling function that ensures the conservation of linear momentum. A review of the engineering wake models that are considered for comparison in the current study is presented in Appendix C, and some supplementary materials are included in Appendix D.

2. Wake model based on the diffusion of a passive scalar

2.1. *Expression for wake shape*

In this section, we present a turbine-wake model based on the analogy between the distribution of a turbine's wake normal to the streamwise direction and the diffusion of a passive scalar from a disk source. Following Crank (1979), the diffusion equation from

a circular disk source with a uniform initial concentration ϑ_o is

$$\frac{\vartheta(t, r)}{\vartheta_o} = \frac{1}{2\mathcal{D}t} \exp(-r^2/(4\mathcal{D}t)) \int_0^{R_d} r' \exp(-r'^2/(4\mathcal{D}t)) \mathrm{I}_0\left(\frac{rr'}{2\mathcal{D}t}\right) \mathrm{d}r', \qquad (2.1)$$

where ϑ is the concentration of the passive scalar, $\mathcal{D}$ is a diffusion coefficient, t is time, R_d is the radius of the disk source, r is the radial distance from the disk's centre and I_ν is the modified Bessel function of first kind and order ν. An analogous expression can be written for a self-similar axisymmetric wake of a wind turbine by introducing the length scale $\sigma = \sqrt{2\mathcal{D}t}$, which varies in the streamwise direction. The notion of time in the case of the diffusion of a passive scalar is equivalent to the distance downstream of a turbine. This means that every time instance of the concentration profile of the passive scalar (2.1) corresponds to the wake distribution normal to the streamwise direction at a specific distance downstream of the turbine, both of which are related through some advection wind speed (Cheng & Porté-Agel 2018). However, the notion of time in the framework of a turbine's wake is irrelevant since we seek a steady-state solution, and we do not adopt Lagrangian approaches which rely on quantifying the time required for a particle to travel from the turbine to a specific distance downstream of the turbine.

Herein, we assume that the normalised wind-speed deficit W takes the form

$$W(x, r) = 1 - \frac{u(x, r)}{u_\infty} = C(x) \exp(-r^2/(2\sigma^2)) \underbrace{\frac{1}{\sigma^2} \int_0^{R_d} r' \exp(-r'^2/(2\sigma^2)) \mathrm{I}_0\left(\frac{rr'}{\sigma^2}\right) \mathrm{d}r'}_{\mathcal{S}(x,r)},$$
$$(2.2)$$

where u is the streamwise wind speed in the wake region, u_∞ is the free-stream wind speed and $C(x)$ is a scaling function that will be determined from the conservation of linear momentum. Note that R_d is the radius of the passive scalar disk source and is generally different from the turbine's radius R (§ 2.5). Also, the introduced length scale σ is not the same as the Gaussian or the super-Gaussian wake widths, but is analogous to these two definitions specific to the assumed wake profile (2.2).

The right-hand side of (2.2) contains a Gaussian function $\exp(-r^2/(2\sigma^2))$ multiplied by a shaping function $\mathcal{S}(x, r)$ whose role is to have a radially uniform profile near to the wake source and a Gaussian profile in the far wake. To show this, we examine the limiting cases of $\mathcal{S}$ when the length scale σ is small (close to the turbine) and when σ is large (far from the turbine). As discussed in Appendix A (A11), for a small σ the shaping function $\mathcal{S}$ can be approximated by $\exp(r^2/(2\sigma^2))$, which cancels out the Gaussian part in (2.2) resulting in a radially uniform deficit profile. Far away from the turbine, σ is large enough to have $\mathrm{I}_0(rr'/\sigma^2) \approx 1$, and hence $\mathcal{S} = \mathcal{S}(x)$ is no longer dependent on the radial coordinate r, making the profile of W defined by the Gaussian part $\exp(-r^2/(2\sigma^2))$. Therefore, the shaping function $\mathcal{S}$ transitions from having an exponential profile (inverse of a Gaussian profile) to having a radially uniform profile away from the turbine. This transition is caused by the decay of $\mathrm{I}_0(rr'/\sigma^2)$ to unity as the wake evolves. Moreover, a similar formulation of (2.2) can be obtained by seeking a rotor-averaged wind-speed deficit for a turbine of radius R_d that is placed in a Gaussian axisymmetric upstream wake and is radially offset from the wake source by a distance r (Ali, Stallard & Ouro 2024b). In this case, the shaping function $\mathcal{S}$ acts as a filter to a background Gaussian field using a circular disk of radius R_d. At a far-enough distance from the turbine, the filter size R_d becomes sufficiently smaller than the wake width so that the filtering process does not affect the Gaussian profile of the upstream wake.

To use the wake description provided in (2.2), the integral in $\mathcal{S}$ needs to be evaluated. This one-dimensional integral can be evaluated using quadrature integration by any mathematical toolbox. However, here, we propose two possible semi-analytical solutions to this integral which require the evaluation of a series, as will be shown. Based on the solution in Appendix A (A7), a possible solution to (2.2) is

$$W(x, r) = C(x) \left(1 - \exp(-R_d^2/(2\sigma^2)) \exp(-r^2/(2\sigma^2)) \sum_{k \geq 0} \left(\frac{r}{R_d} \right)^k \mathrm{I}_k \left(\frac{rR_d}{\sigma^2} \right) \right), \quad (2.3)$$

which can also be written in terms of the Marcum Q-function (A9) as

$$W(x, r) = C(x)(1 - Q_1(r/\sigma, R_d/\sigma)). \quad (2.4)$$

When σ is small (i.e. close to the turbine) the summation over k in (2.3) may require a large number of evaluations of modified Bessel functions to converge, although the recursive property of the modified Bessel function should be employed in this case (Abramowitz & Stegun 1972, p. 376; 9.6.26). Also, the Marcum Q-function may not be available in all mathematical toolboxes. Alternatively, we can use the solution presented by Ali *et al.* (2024*b*) based on the tables by Rosenheinrich (2017) to obtain

$$W(x, r) = C(x) \exp(-R_d^2/(2\sigma^2)) \exp(-r^2/(2\sigma^2))\Psi \left(\frac{r}{R_d}, \frac{\sigma}{R_d} \right), \quad (2.5)$$

where $\Psi = \mathcal{S} \exp(R_d^2/(2\sigma^2))$ is defined as

$$\Psi(\zeta_1, \zeta_2) = \mathrm{I}_0 \left(\frac{\zeta_1}{\zeta_2^2} \right) \sum_{k \geq 1} \left(\frac{f_k(\zeta_1/\zeta_2)}{(2\zeta_2^2)^k} \right) - \frac{\zeta_1}{\zeta_2^2} \mathrm{I}_1 \left(\frac{\zeta_1}{\zeta_2^2} \right) \sum_{k \geq 1} \left(\frac{g_k(\zeta_1/\zeta_2)}{(2\zeta_2^2)^k} \right), \quad (2.6)$$

and the coefficients f_k and g_k satisfy the recursions

$$f_k(\alpha) = \frac{f_{k-1}(\alpha) + \alpha^2 g_{k-1}(\alpha)}{k}, \quad g_k(\alpha) = \frac{f_k(\alpha) + 2g_{k-1}(\alpha)}{2k}, \quad (2.7a,b)$$

with $f_0 = 1$ and $g_0 = 0$. The summations in (2.6) converge rapidly in less than 10 iterations of simple algebraic operations (2.7*a*,*b*), and (2.6) requires only two evaluations of the modified Bessel function, which makes it computationally more efficient than (2.3). A Python implementation of (2.6) and (2.7*a*,*b*) is available at Ali, Stallard & Ouro (2024*a*).

2.2. *Conservation of linear momentum*

To obtain an expression for the scaling function C (2.2), we make use of the integral form of the conservation of linear momentum for an axisymmetric wake (Tennekes & Lumley 1972)

$$2\pi\rho \int_0^\infty u(u_\infty - u)r \, \mathrm{d}r = \tfrac{1}{2}\rho C_t \pi R^2 u_\infty^2, \quad (2.8)$$

where ρ is air density, and C_t is the thrust coefficient of the wind turbine. Detailed derivations to solve (2.8) are available in Appendix B. Equation (2.8) can be

simplified to

$$\underbrace{\int_0^\infty rW \, \mathrm{d}r}_{A_1} - \underbrace{\int_0^\infty rW^2 \, \mathrm{d}r}_{A_2} = R^2 C_t/4. \tag{2.9}$$

Following the solution in Appendix B, we have $A_1 = R_d^2 C/2$ and $A_2 \approx R_d^2 C^2 \Lambda/4$, where

$$\Lambda = 2 \left(\mathrm{erf}\left(\frac{R_d}{\sigma}\right) - \frac{\sigma}{\sqrt{\pi}R_d} \left(1 - \exp(-R_d^2/\sigma^2)\right) \right)^2, \tag{2.10}$$

with erf being the error function (Ng & Geller 1969; Ali, Stallard & Ouro 2024c). We used an approximation sign for A_2 because Λ was not derived directly from A_2 but from an alias of A_2 (see Appendix B for more details). Therefore, (2.9) can be solved for C as

$$C \approx \frac{1 - \sqrt{1 - (R/R_d)^2 \Lambda C_t}}{\Lambda}. \tag{2.11}$$

To complete the model, expressions for the source disk radius R_d and the length scale σ are needed. Thus far, no assumptions were made about the length scale σ, making (2.2), along with its solutions (2.3)–(2.5), and the scaling function (2.11) generic for any $\sigma(x)$.

2.3. *Far-wake expansion*

Far from the wake source, high-fidelity simulations and experimental measurements of turbine wakes in turbulent flows show that wakes expand almost linearly in the streamwise direction with a rate that is proportional to the free-stream turbulence intensity (Porté-Agel, Bastankhah & Shamsoddin 2020). Multiple linear expressions have been suggested in the literature based on fitting high-fidelity data (e.g. Bastankhah & Porté-Agel 2014; Carbajo Fuertes, Markfort & Porté-Agel 2018; Cathelain *et al.* 2020). Herein, we use the linear expression suggested by Cathelain *et al.* (2020), which provided the best performance against simulations and measurements when combined with (2.2) and (2.11), as shown later in § 3. There are no restrictions to use an expression that was obtained for a super-Gaussian model here with a diffusion-based model (2.2) as long as it is applied in the far wake only, since both the proposed model and the super-Gaussian model approach a Gaussian form far enough downstream (see figure 8). Following Cathelain *et al.* (2020), the far-wake length scale σ_{fw} is defined as

$$\sigma_{fw} = \underbrace{(0.0119 + 0.18 \, T_i)}_{k^*} x + \underbrace{(0.13 + 0.0564 \, C_t) \sqrt{\beta}}_{\varepsilon} D, \tag{2.12}$$

where T_i is the free-stream turbulence intensity, k^* is the rate of expansion in the far wake and D is the rotor's diameter. In linear-expansion models, the parameter ε represents the initial wake width at $x = 0$, and the constant β is defined as

$$\beta = \frac{1 + \sqrt{1 - C_t}}{2\sqrt{1 - C_t}}. \tag{2.13}$$

Due to differences in the flow structure between the near-wake and the far-wake regions (discussed in § 2.4), (2.12) is only applied to the far-wake region, and some modifications are made to σ_{fw} to suit the near wake as follows.

1001 A13-6

2.4. *Near-wake treatment*

The near wake is a region of complex structures that are challenging to model analytically. The structure of the flow within this region is three-dimensional, non-symmetric and highly influenced by the geometry of the turbine and the operating tip-speed ratio (Bastankhah & Porté-Agel 2017). Although adopting engineering wake models in the near wake should be handled with caution, as the assumption of self-similarity is not theoretically valid in this region, we attempt to modify the linear expansion of the far-wake length scale σ_{fw} (2.12) to approximate the near-wake deficit shape and evolution. The streamwise extent of the near wake has been addressed in multiple studies (e.g. Vermeulen 1980; Sørensen *et al.* 2014, 2015; Bastankhah & Porté-Agel 2016). Herein, we adopt the formulation of the near-wake length x_o suggested by Bastankhah & Porté-Agel (2016) following Lee & Chu (2003) for a non-yawed turbine

$$\frac{x_o}{D} = \frac{1 + \sqrt{1 - C_t}}{\sqrt{2}\left(4c_1 T_i + c_2\left(1 - \sqrt{1 - C_t}\right)\right)}, \tag{2.14}$$

where $c_1 = 0.58$ and $c_2 = 0.154$.

Downstream of a turbine, a free-shear layer is formed between the free-stream flow and the waked flow due to the drop in pressure and wind speed caused by the turbine's momentum extraction (Posa & Broglia 2021). The evolution of this shear layer depends on the strength and stability of the tip vortices shed by the blades, which partially shield the waked flow from the free-stream flow by reducing momentum and mass transfer across the shear layer (Ivanell *et al.* 2010). If, hypothetically, the tip vortices were to be modelled as an elastic tube that perfectly insulates the waked flow from the free-stream flow, then the pressure difference across this elastic tube would cause the tube to contract, assuming an infinitely long tube in the streamwise direction. However, this does not occur for a turbine's wake as the tip vortices do not perfectly prevent any mass and momentum transfer, leading to a relatively quick pressure recovery shortly downstream of the turbine. On the other hand, a free-shear layer with no resistance for mass and momentum transfer across the layer would have a relatively faster expansion than a shear layer with some resistance. Based on this, we propose an expression for the near-wake length scale σ_{nw} as a superposition of a contraction tendency (in case of perfect wake insulation) and an expansion tendency (in case of no wake insulation)

$$\sigma_{nw} = \underbrace{\varepsilon R_d \exp(-x/(\tau x_o))}_{contraction} + \underbrace{\sigma_{fw}\left(R_d/R\right)\exp(-R^2/(2\sigma_{fw}^2))}_{expansion}, \tag{2.15}$$

where $\tau = 2$, the far-wake length scale σ_{fw} and the parameter ε are defined in (2.12), the near-wake length x_o is given by (2.14), R_d is the radius of the source disk and R is the turbine's radius. It is crucial to note that (2.15) is an empirical expression structured to be used specifically with the expression for the far-wake length scale σ_{fw} (2.12) and the proposed wake shape (2.2). A generic expression for the near-wake length scale σ_{nw} obtained from first principles is beyond the scope of the current study. Furthermore, the parameter τ in the contraction term of (2.15) was obtained through trial and error against the LES deficit profiles included in § 3 (figure 4), while noting that the model's predictions were not very sensitive to τ since it only affects the shape of the near wake but has small effect on the far wake (see examples in Appendix D).

Finally, the overall length scale σ is obtained by combining (2.12) and (2.15) using

$$\sigma(x) = \begin{cases} \sigma_{nw} & \text{if } x \le x_o, \\ \sigma_{fw} - \exp(\tau(1 - x/x_o))\left(\sigma_{fw} - \sigma_{nw}\right) & \text{if } x > x_o. \end{cases} \tag{2.16}$$
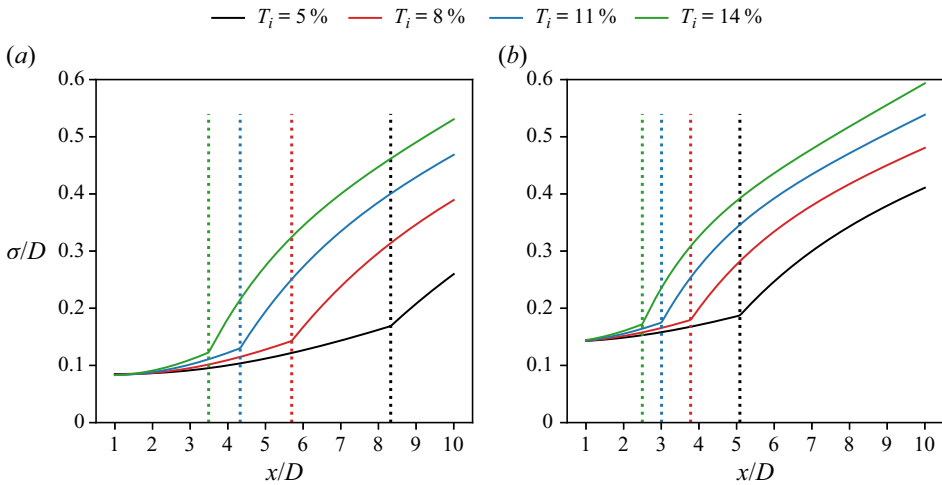
1001 A13-7

Figure 1. The streamwise variation of the length scale σ following (2.16) for (*a*) $C_t = 0.4$ and (*b*) $C_t = 0.8$ at different turbulence intensities (T_i) from 5 % to 14 %. The vertical dotted lines are the near-wake lengths as predicted by (2.14).

Similar to (2.15), the suggested blend in (2.16) for $x > x_o$ is empirical and is designed to be used specifically with the expressions for the near- and far-wake length scales (2.15) and (2.12) and the proposed wake shape (2.2).

The streamwise variation of the length scale σ (2.16) is shown in figure 1 for low ($C_t = 0.4$) and high ($C_t = 0.8$) turbine thrust coefficients at different free-stream turbulence intensities. The corresponding near-wake lengths x_o (2.14) are shown by vertical dotted lines for each case. Similar to high-fidelity observations (e.g. Troldborg, Sorensen & Mikkelsen 2010), the rate of wake expansion in the near wake (2.15) is slower than that in the far wake (2.12), with the high turbulence cases having higher recovery rates and shorter near-wake regions (figure 1). Moreover, figure 8 (Appendix D) shows the difference between the adopted length scale σ (2.16) and the far-wake length scale σ_{fw} (2.12) for one of the cases in figure 1. As previously indicated, σ_{fw} is used only in the very-far wake where both the proposed wake model (2.2) and the super-Gaussian model of Cathelain *et al.* (2020, who developed the expression for σ_{fw} in (2.12)) approach a Gaussian wake profile (at $x/D \sim 8$ for the case in figure 8). Otherwise, the near-wake length scale σ_{nw} (2.15) and the exponential blend between σ_{nw} and σ_{fw} (2.16) set the difference between the adopted length scale σ and the far-wake length scale σ_{fw}. Having obtained an expression for the length scale σ, a solution to (2.2) requires a definition for the radius of the source disk R_d, which is discussed in the next section.

2.5. *Source disk radius*

To have an expression for the source disk radius R_d, we rely on one-dimensional momentum theory by assuming that the pressure recovers quickly to its free-stream value a short distance downstream of the turbine, i.e. when $x \sim 0$ (Narasimhan, Gayme & Meneveau 2024). This is a simplifying assumption, because in reality the pressure recovers after a finite distance downstream of the turbine, along which the wake expands slightly from its initial size (the turbine's size). Modelling the pressure-recovery region within the proposed low-fidelity wake model is not straightforward, and so this initial wake expansion
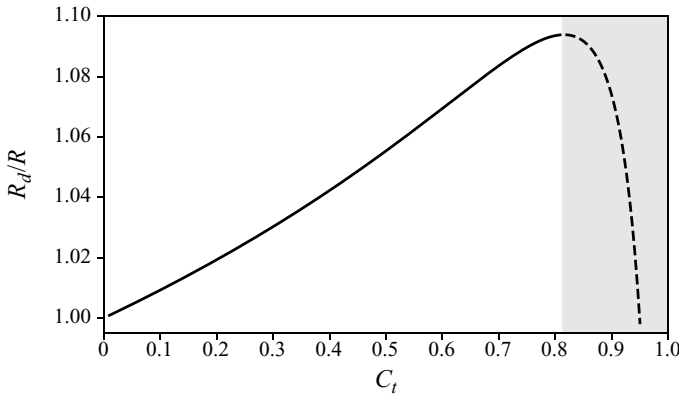
Figure 2. The variation of the ratio between the source disk radius R_d and the turbine radius R (2.18) with the thrust coefficient C_t. The shaded region is where the one-dimensional momentum theory becomes impractical by predicting very low wind speeds (very high deficits approaching 100 %) downstream of the turbine, and is typically replaced by empirical expressions.

is modelled in a similar manner to Blondel & Cathelain (2020) by increasing the size of the source disk.

At $x = 0$, the wake's profile normal to the streamwise direction is fairly uniform, so that we can use the centreline deficit (i.e. $r = 0$). From one-dimensional momentum theory, the normalised wind-speed deficit (W) when the pressure recovers to its free-stream value (here at $x = 0$) is $1 - \sqrt{1 - C_t}$ (Burton *et al.* 2021), which can be equated to the exact solution of (2.2) at the centre of the wake

$$C_o \left(1 - \exp(-R_d^2/(2\sigma_o^2)) \right) = 1 - \sqrt{1 - C_t}. \tag{2.17}$$

In (2.17), $C_o = C(0)$ and $\sigma_o = \sigma(0)$ are the scaling function C and the length scale σ just downstream of the turbine, respectively. We can use (2.11) at $x = 0$ to solve for the disk radius

$$R_d/R = \sqrt{\frac{C_t}{C_o (2 - \Lambda_o C_o)}}, \tag{2.18}$$

where $\Lambda_o = \Lambda(0)$ can be evaluated from (2.10) by replacing σ/R_d with σ_o/R_d which is known from (2.15)

$$\sigma_o/R_d = \varepsilon \left(1 + 2 \exp(-1/(8\varepsilon^2)) \right). \tag{2.19}$$

Similarly, C_o is given by (2.17) by employing (2.19). From (2.18), the ratio R_d/R is dependent on the thrust coefficient C_t only, and this dependency is shown in figure 2, which indicates that the source disk radius R_d is at most approximately 9 % larger than the turbine's radius which occurs at $C_t \sim 0.81$. At higher thrust coefficients, the required disk radius to satisfy the one-dimensional momentum theory (2.17) decreases until it reaches a value of 1 at $C_t \sim 0.95$, after which (2.17) cannot be satisfied. In the shaded region of figure 2, the one-dimensional momentum theory is often replaced by empirical expressions for the relation between the thrust coefficient and the axial induction of the turbine (e.g. Glauert 1926; Buhl 2005; Burton *et al.* 2021; Liew, Heck & Howland 2024), because the momentum theory predicts very low wind speeds downstream of the turbine (deficit

approaching 100 %) which is not physical. However, this is beyond the scope of the current study, and we suggest limiting (2.18) to values of C_t up to 0.9.

2.6. *Summary of the proposed model*

Thus far, we have determined expressions for all the variables required to solve for the deficit W (2.2). To summarise, the input data of the proposed wake model are the turbine's thrust coefficient C_t, the free-stream turbulence intensity T_i and the turbine's rotor radius R. The model predicts the streamwise and radial distributions of the wind-speed deficit downstream of the turbine based on the following steps.

(i) Calculate the source disk radius R_d.
   (a) From (2.19), calculate the ratio σ_o/R_d using the definition of ε in (2.12).
   (b) Evaluate Λ_o (2.10) and C_o (2.17) using the ratio σ_o/R_d obtained above.
   (c) Using Λ_o and C_o, the radius of the source disk R_d can be obtained from (2.18).
(iii) Calculate the length scale σ.
   (a) Calculate the far-wake length scale σ_{fw} from (2.12), where the constant β is obtained from (2.13).
   (b) The near-wake length x_o is obtained from (2.14).
   (c) Calculate the near-wake length scale σ_{nw} from (2.15).
   (d) The length scale σ can be obtained from (2.16) based on the streamwise distance x from the turbine relative to the near-wake length x_o.
(iii) Calculate the streamwise scaling function $C(x)$.
   (a) Evaluate Λ from 2.10 using the values for σ and R_d obtained above.
   (b) Use (2.11) to calculate the function $C(x)$.
(iv) Evaluate the radial distribution of the deficit $W(x, r)$ using one of the following options.
   (a) Numerically approximate (2.2) using quadrature integration.
   (b) Use the series solution in (2.3).
   (c) If the Marcum Q-function is accessible via the used mathematical toolbox, use (2.4).
   (d) Use the solution of W in (2.5) with the aid of the function Ψ (2.6), which depends on the recursions in (2.7a,b).

3. Validation

In this section, we compare the results of the wake model presented in § 2 with LES and experimental data. Rather than performing a special set of simulations and/or experiments to provide reference data for validation, we employ published numerical and experimental datasets from different research groups.

The first dataset is the LES results of a wind turbine obtained by Vahidi & Porté-Agel (2022) with an in-house LES code using an actuator disk model in a neutral atmospheric boundary layer flow. They performed a set of simulations for a range of T_i (5.3 %–14 %) while keeping C_t nearly constant at a value of 0.8. The results of these simulations are labelled 'EPFL-LES'. The second set is the experimental measurements used by Blondel & Cathelain (2020) for their validation based on the experiments by Aubrun *et al.* (2013) of a model porous disk in isotropic turbulence, where measurements were taken using wire probes. The experiments comprised cases with high (12 %) and low (5 %) turbulence intensities for different values of C_t within the range 0.45–0.73. We also use the experimental measurements reported by Schreiber *et al.* (2020) based on Wang *et al.* (2017) for a model turbine operating at $C_t = 0.75$ in a free-stream turbulence intensity of

5 %, where wake measurements were obtained using hot-wire probes and particle image velocimetry. Using these datasets, the present model is compared with the Gaussian model of Bastankhah & Porté-Agel (2014, hereafter BPA14), and the super-Gaussian models of Blondel & Cathelain (2020, hereafter B20), Cathelain *et al.* (2020, hereafter C20) and Blondel (2023, hereafter B23). The details of these models are summarised in Appendix C. It should be noted that the Gaussian model (BPA14) is intended to be used only in the far wake. Therefore, its predictions in the near wake are included for comparison only.

Figure 3 presents a comparison of the hub-height normalised wind-speed deficit predicted by the present model along with the previously mentioned models against the EPFL-LES data. The streamwise variation of the maximum deficit for the same cases of figure 3 is shown in figure 4. The comparison indicates that the present model (black curves) agrees well with the LES results in the near- and far-wake regions. The largest deviations from the LES results are a slight overestimation of the near-wake width in the highest turbulence case (figure 3*a*), and a slight overestimation of the far-wake deficit in the lowest turbulence case (figure 3*s*,*t*). For all other locations, the wake profiles predicted with the new diffusion-based model are in excellent agreement with the LES, and it is noted that none of the considered models capture the observed behaviour in the far wake for the lowest turbulence case (figure 3*s*,*t*).

Figure 4 shows that the near-wake formulation of the length scale σ introduced in § 2.4 captures the transition from a low recovery rate in the near-wake region to faster recovery further downstream. It is noted that the maximum deficit predicted by the present model is slightly less than that of the LES in the near-wake region of the low turbulence cases (figure 4*d*,*e*). This is expected as the maximum deficit in the near-wake region is typically offset from the wake centreline (figure 3*m*,*q*), but the present model as well as all the considered models has the maximum deficit at the centre of the wake. Figure 4 shows that the B20 and B23 models were calibrated to match the profiles of the centreline deficit rather than the maximum deficit because both predict an initial increase in the maximum wind-speed deficit rather than the monotonic decrease in the maximum deficit close to the turbine as predicted by LES (e.g. figure 4*e*). Matching the behaviour of the centreline deficit with a model that does not include the lateral offset of the maximum deficit from the wake centreline can lead to an underestimation of the deficit in the near wake by incorrectly matching the maximum deficit to the centreline deficit. To include the radial offset of the maximum deficit away from the wake centreline in the proposed diffusion-based model, the initial distribution of the passive scalar across the source disk would need to be non-uniform. However, this is beyond the scope of the current study.

Because it is not designed for the near wake, the BPA14 model (blue curves) deviates substantially from LES data in the near-wake region of the cases with $T_i = 9.9\,\%$ (figure 3*e*) and $T_i = 7.7\,\%$ (figure 3*i*), and is not applicable for the cases with $T_i = 6.2\,\%$ (figure 3*m*) and $T_i = 5.3\,\%$ (figure 3*q*) because of having $\sigma_g < R\sqrt{C_t/2}$ (C2). However, for $x \geq 6D$, the Gaussian model matches the deficit of the LES data well except for the cases of high turbulence, where it slightly underestimates the deficit (figure 3*b*,*f*). The B20 model (green curves) overestimates the deficit compared with LES in all of the cases and at almost all locations downstream of the turbine except in the near-wake region of the low turbulence cases (figures 3*m*,*q* and 4*b*–*e*). The model also underestimates the deficit in the near-wake region of the high turbulence cases (figure 3*a*,*e*,*i*). However, the re-calibration of this model as presented by the B23 model (dashed-green curves) enhances the model's predictions significantly. Nonetheless, the B23 model overestimates the far-wake deficit
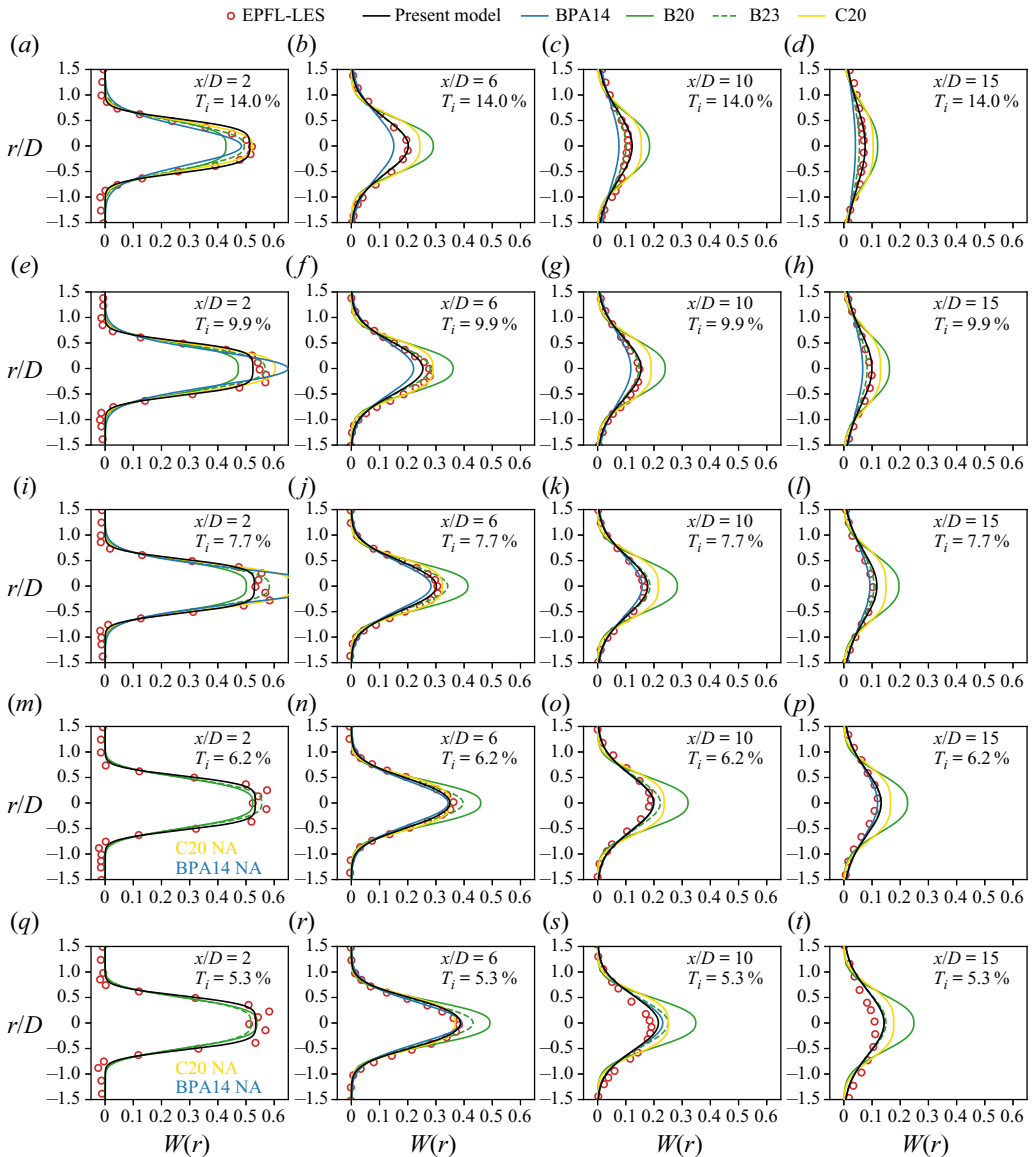
Figure 3. A comparison of hub-height lateral profiles of the normalised wind-speed deficit for different distances downstream against LES results (red circles) obtained from Vahidi & Porté-Agel (2022), between the present wake model (black curves), the Gaussian wake model (blue curves) of Bastankhah & Porté-Agel (2014) and the super-Gaussian wake models of Blondel & Cathelain (2020) shown by solid-green curves (B20), Cathelain *et al.* (2020) shown by yellow curves (C20) and Blondel (2023) shown by dashed-green curves (B23). All the shown cases have $C_t = 0.8$. Each row represents a case with a different turbulence intensity as indicated. Whenever a model fails in one of the cases, its abbreviation is written with the label 'NA', which stands for 'not applicable'.

for the low turbulence case (figure 3*r–t*). Finally, the C20 model (yellow curves) generally overestimates the deficit for the high turbulence cases (figures 3*b–d*, *f–h* and 4*a,b*), except in the near wake where it matches the LES data well (figure 3*a*). Similar to the Gaussian model, the C20 model is not applicable in the near wake of the low turbulence cases because the quantity in the square root in (C8) is negative.
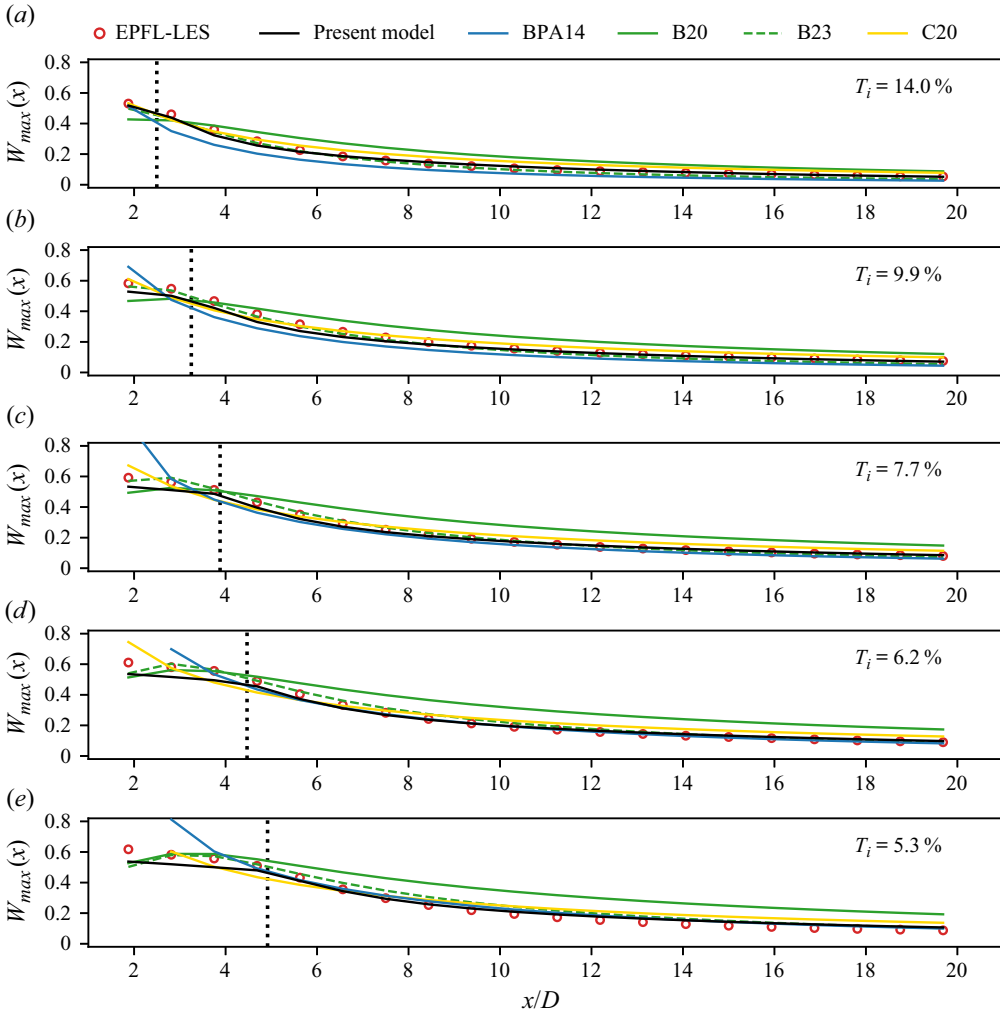
1001 A13-12

Figure 4. Comparing the streamwise variation of the maximum normalised wind-speed deficit $W_{max}(x)$ against the LES results of Vahidi & Porté-Agel (2022). The compared models, and their colours, are the same as in figure 3. The vertical dotted lines represent the location of the near wake of each case as defined by (2.14).

Figure 5 shows a similar comparison as that in figure 3 but against the porous-disk experiments of Aubrun *et al.* (2013) for a combination of high and low values of C_t and T_i. The present model (black curves) matches the experiments well in all of the cases except in the far wake, where the deficit is underestimated (figure 5*h*,*l*,*p*). However, all the considered models underestimate the far-wake deficit except the B20 model which was calibrated to match this dataset. Also, the present model better captures the wake width compared with the other models, which underestimate the wake width in some of the cases (e.g. figure 5*b*,*c*,*e*,*f*). The discrepancies between the present model and the porous-disk measurements can be partially attributed to the adopted model of near-wake length x_o (2.14) that is calibrated for the wakes of wind turbines (Bastankhah & Porté-Agel 2016). Using different values for c_1 and c_2 in (2.14) can mitigate these discrepancies. However, when compared with the experimental measurements of a three-bladed turbine (see figure 6), the proposed model gave good predictions.
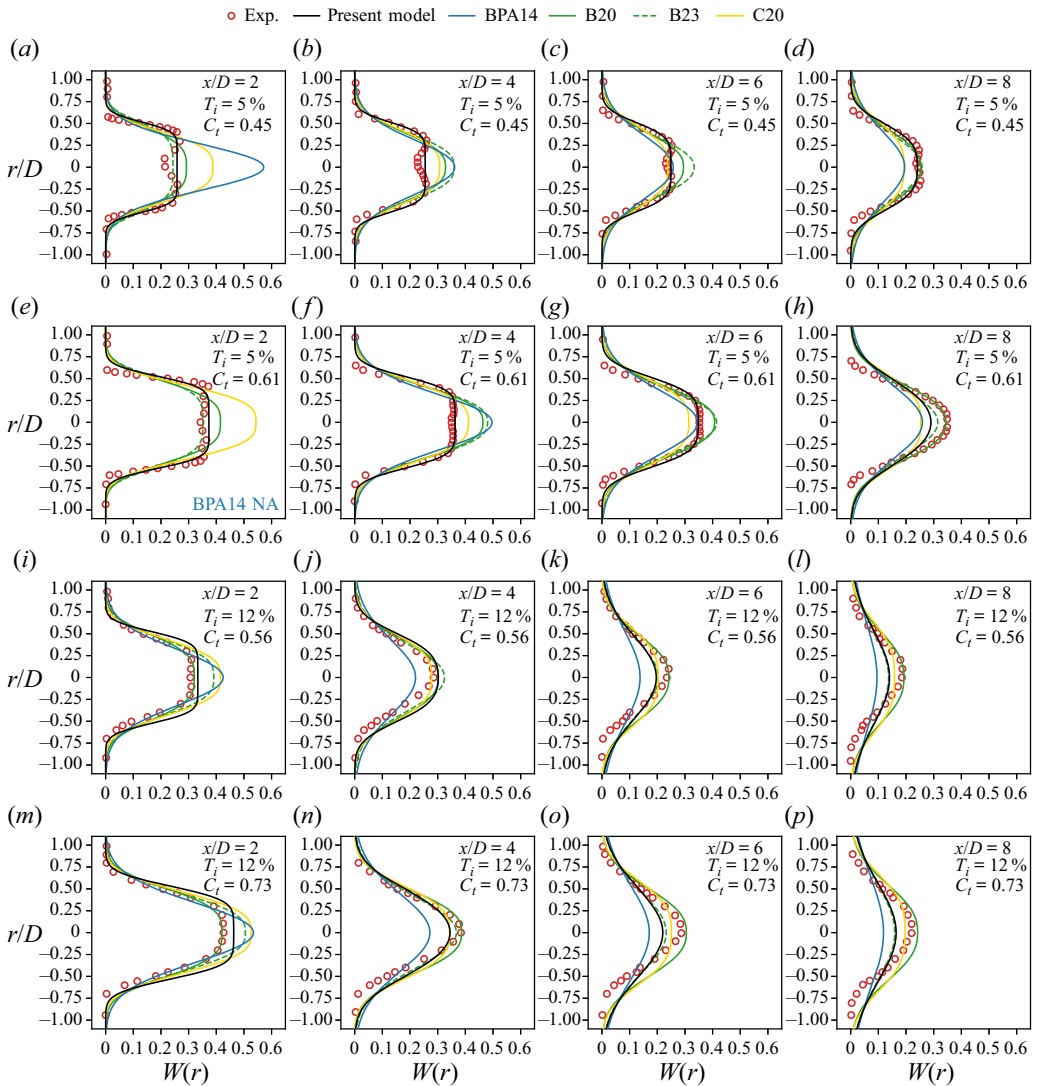
Figure 5. Comparing the lateral profiles of the normalised wind-speed deficit of the present model (black curves) and the other Gaussian and super-Gaussian models mentioned in figure 3 with the porous-disk experiments (red circles) of Aubrun *et al.* (2013). Each row represents a case with its C_t and T_i as indicated, whereas each column is a specific location downstream of the wake source. Whenever a model fails in one of the cases, its abbreviation is written with the label 'NA', which stands for 'not applicable'.

Similar to the LES results in figure 3, the BPA14 model performs poorly in the near wake of the low T_i and low C_t case (figure 5a), and is not applicable for the low T_i and high C_t case (figure 5e). Also, the BPA14 model underestimates the deficit in the high turbulence cases (third and fourth rows of figure 5), except in the near wake, where it slightly overestimates the deficit (figure 5i,m). The B20 model captures the deficit well in the near wake of the low turbulence case (figure 5a,e), but overestimates the deficit at $x = 4D$ (figure 5b,f) and $x = 6D$ (figure 5c,g). The B23 model did not enhance the accuracy of the B20 model in this dataset, but gave worse results in the near wake of the high turbulence cases (figure 5i,m). The C20 model consistently overestimates the deficit in
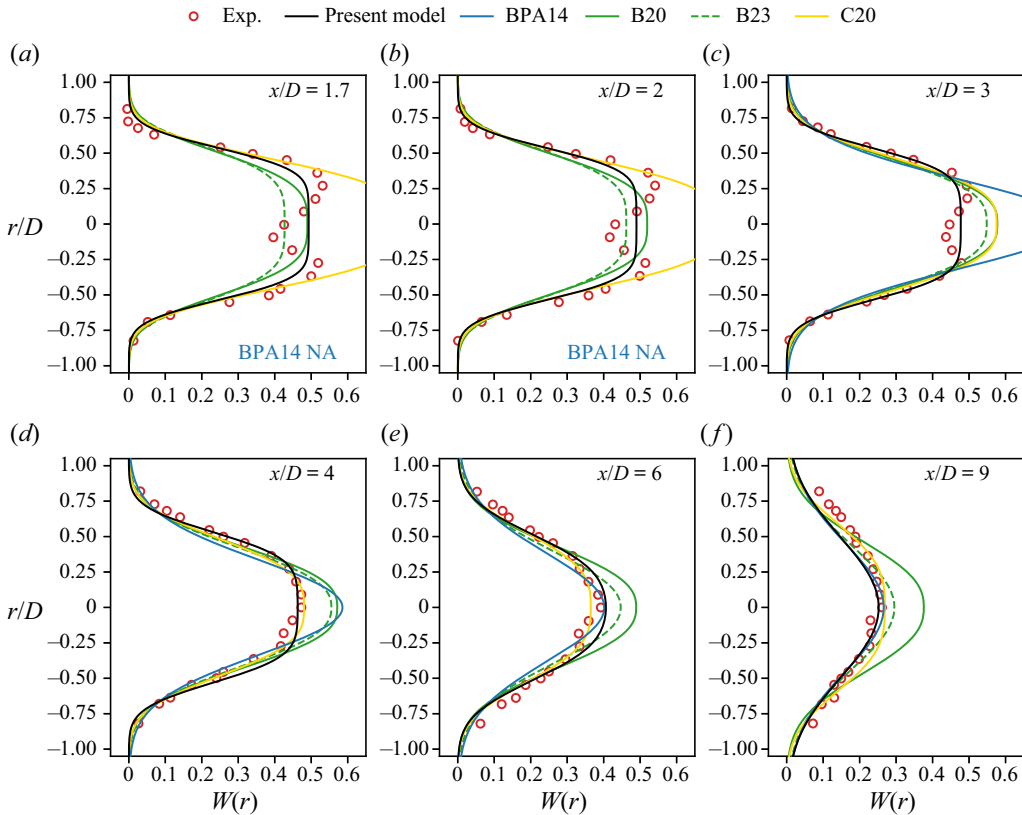
Figure 6. Comparing the lateral profiles of the normalised wind-speed deficit of the present model (black curves) and the other Gaussian and super-Gaussian models mentioned in figure 3 with the measurements in the wake of a model G1 turbine done by Wang *et al.* (2017) and reported by Schreiber *et al.* (2020). The model turbine operated at $C_t = 0.75$ in a free-stream turbulence intensity of 5%. Each panel represents a specific location downstream of the turbine as indicated. Whenever a model fails in one of the cases, its abbreviation is written with the label 'NA', which stands for 'not applicable'.

the near wake of all the cases of this dataset (first column of figure 5), and underestimates the deficit in the far wake of the low turbulence cases (figure 5*d,h*).

The last considered dataset is the experimental measurements of a three-bladed turbine (Wang *et al.* 2017), which are presented in figure 6 comparing the lateral profiles of the normalised deficit for the considered wake models (same as in figure 3). The present model captures both the width and the magnitude of the deficit profiles well compared with the experimental measurements (figure 6). As this experiment is at low T_i and high C_t, the BPA14 model is not applicable in the near wake (figure 6*a,b*), and overestimates the deficit significantly at $x = 3D$ (figure 6*c*) and $x = 4D$ (figure 6*d*). However, the model captures the wake profile well in the far wake (figure 6*f*). The B20 model captures the magnitude of the deficit well in the near wake but underestimates the width of the wake (figure 6*a,b*), after which the model consistently overestimates the deficit magnitude (figure 6*c–f*). The re-calibration in the B23 model did not improve the performance of the B20 model in the near wake, as the B23 model underestimates both the magnitude and the width of the wake (figure 6*a,b*). The overestimation of the deficit magnitude just after the near wake still persists for the B23 model compared with the B20 model and to the experimental measurements (figure 6*c,d*), but the overestimation of the deficit in the very far wake is significantly enhanced for the B23 model (figure 6*e,f*). The C20 model

deviates significantly from the experimental measurements in the near wake (figure 6*a–c*), but performs well in the far wake (figure 6*d–f*).

4. Discussion

From the validation results shown in § 3, the proposed wake model has been shown to be the most consistent when compared with the reference data of the considered experimental and LES datasets, whereas the other wake models performed well in some cases and poorly in other cases, yielding larger uncertainty. Nonetheless, the diffusion-based model coupled with the expansion model in (2.12) underestimated the far-wake deficit of the high turbulence cases in the porous-disk experiments (figure 5*l*,*p*). This discrepancy is partially due to using a near-wake length model (2.14) that is calibrated for turbine wakes, which is supported by the better performance of the proposed model when compared with the measurements in the wake of a three-bladed turbine (figure 6).

It should be noted that the super-Gaussian models, which rely on a set of tuning parameters obtained from fitting high-fidelity data, perform well in the datasets that were included in their calibration process but their accuracy can deteriorate in other datasets. For instance the B20 model performed better than the B23 model in the dataset shown in figure 5 but worse in figures 3 and 6. The C20 model provided good accuracy in the far wake of the high turbulence cases but performed poorly in the near wake, especially for the low turbulence cases. Even the BPA14 model, coupled with the expansion model in (C4), overestimated the wake recovery in the far wake of the high turbulence cases. In contrast, the proposed diffusion-based model matched LES data and experimental measurements, with an acceptable accuracy for a low-fidelity engineering wake model, in both the near- and far-wake regions of all the considered cases with low/high turbulence and low/high turbine thrust coefficients.

The suggested form of the deficit equation (2.2), along with the suggested solutions (2.3)–(2.5) and the streamwise scaling function (2.11) are generic expressions in the sense that they do not depend on any empirical relations. Modelling σ is, however, empirical. The linear expansion of the length scale σ in the far wake (2.12) is empirical based on fitting high-fidelity data. Analogously, the near-wake modification discussed in § 2.4 is empirical, as it was not derived from first principles. The condition for obtaining the radius of the source disk (2.17) is also generic as it was obtained from the suggested deficit equation (2.2) and the one-dimensional momentum theory. However, converting this condition to an expression for R_d as a function of the turbine's thrust coefficient depends on the empirical expressions of σ_{fw} (far-wake length scale; (2.12)) and σ_{nw} (near-wake length scale; (2.15)).

The presented combination of these generic and empirical expressions provides consistent and accurate-enough predictions for a low-fidelity wake model, and outperforms current engineering wake models from the literature for a wide range of turbulence intensities and turbine thrust coefficients. All the considered validation cases in the current study were of a single wake. Nonetheless, the proposed model can be extended to a wind farm by using various wake-superposition methods (e.g. Voutsinas, Rados & Zervos 1990; Niayifar & Porté-Agel 2015; Bastankhah *et al.* 2021) and turbine-induced turbulence models (e.g. Crespo & Hernandez 1996). However, we did not include a validation case for a wind farm as farm results are largely influenced by the used wake-superposition method, and the intent of the current study is not to compare superposition methods.

The mathematical analogy between the suggested deficit equation (2.2), and the rotor-averaged deficit of a turbine in a Gaussian axisymmetric upstream wake (Ali *et al.* 2024*b*) suggests that the turbine's impact on the flow can be depicted as a moving circular

filter through a Gaussian field. The shape of the resulting wake from the filtered field depends on the relative size of the filter and the length scale of the Gaussian field. Far enough from the turbine the filtering process has no effect on the wake shape (i.e. the wake is similar to the Gaussian field), but close to the turbine the filtering process defines the shape of the wake. This way of perceiving the evolution of the wake shape allows for the modelling of more complex wake profiles, such as a double-Gaussian profile, within the same framework of a diffusion-based description of the wake by altering the radial uniformity of the moving filter. In that sense, the Gaussian field is a potential field for different wake shapes and sizes depending on the shape, size and nature of the applied filter.

5. Summary

A new engineering wake model was presented and validated based on the analogy between the profile of a turbine's wake normal to the streamwise direction and the diffusion of a passive scalar from a disk source. The proposed model guarantees that linear momentum is conserved at all locations downstream of the turbine, and it naturally takes into account the evolution of the wake shape from a top-hat profile in the near wake to a Gaussian profile far downstream of the turbine. The model relies on a far-wake linear-expansion model from the literature, but introduces further adjustments to this linear expansion to describe the lower rate of wake expansion observed in the near-wake region. The size of the source disk of the passive scalar is determined from one-dimensional momentum theory based on the assumption of a fully recovered pressure field over a short distance downstream of the turbine.

Three datasets were used to validate the proposed wake model, including high-fidelity LES data and experimental measurements in the wake of a porous disk and a model turbine. The diffusion-based model captured the wake profiles and the streamwise evolution of the maximum deficit well when compared with the reference datasets, with a slight deviation against the far-wake porous-disk measurements in the case of high free-stream turbulence. A comparison with other widely used engineering wake models from the literature, including Gaussian and super-Gaussian models, showed that the new diffusion-based wake model offers a more consistent performance over a wide range of turbulence intensities and turbine thrust coefficients. Super-Gaussian wake models performed well when applied to datasets that were included in their calibration process, but reduced performance is observed when applied to other datasets.

Importantly, the streamwise evolution of the wake shape is accounted for in the proposed model through a physics-based principle (wake diffusion normal to the streamwise direction) rather than an empirical super-Gaussian exponent. Wake models in the literature typically assume a constant deficit in the near-wake region, whereas the introduced empirical expression for near-wake expansion is not restricted to this simplification and is better aligned with LES near-wake results. The presented framework in this study can be extended to more complex wake shapes to account for the near-wake radial offset of the maximum deficit by controlling the initial distribution of the passive scalar. The analytical solutions presented in the current study are not exclusive to turbine wakes but are useful to other applications relying on similar integrals.

Author ORCIDs.

Karim Ali https://orcid.org/0000-0003-4198-5128;

Tim Stallard https://orcid.org/0000-0003-2164-1133;

Pablo Ouro https://orcid.org/0000-0001-6411-8241.

Appendix A. Emphasis on the integral in the diffusion equation

In this appendix, we present a series solution to the integral in (2.2). First, we make use of the improper version of the integral to write (Gradshteyn & Ryzhik 2007, p. 707; 6.633-4)

$$\int_0^\infty r' \exp(-r'^2/(2\sigma^2)) \mathrm{I}_0\left(\frac{rr'}{\sigma^2}\right) \mathrm{d}r' = \sigma^2 \exp(r^2/(2\sigma^2)), \tag{A1}$$

which we can use to re-write the integral of interest as

$$\int_0^{R_d} r' \exp(-r'^2/(2\sigma^2)) \mathrm{I}_0\left(\frac{rr'}{\sigma^2}\right) \mathrm{d}r'$$
$$= \sigma^2 \exp(r^2/(2\sigma^2)) - R_d^2 \underbrace{\int_1^\infty r'' \exp(-r''^2 R_d^2/(2\sigma^2)) \mathrm{I}_0\left(\frac{rr'' R_d}{\sigma^2}\right) \mathrm{d}r''}_{\mathcal{G}}, \tag{A2}$$

where $r'' = r'/R_d$. We can also make use of the multiplication theorem of the modified Bessel function (Abramowitz & Stegun 1972, p. 377; 9.6.51) to write

$$\mathrm{I}_0\left(\frac{rr'' R_d}{\sigma^2}\right) = \sum_{k \geq 0} \frac{1}{k!} \left(r''^2 - 1\right)^k \left(\frac{rR_d}{2\sigma^2}\right)^k \mathrm{I}_k\left(\frac{rR_d}{\sigma^2}\right), \tag{A3}$$

and hence

$$\mathcal{G} = \sum_{k \geq 0} \frac{1}{k!} \left(\frac{rR_d}{2\sigma^2}\right)^k \mathrm{I}_k\left(\frac{rR_d}{\sigma^2}\right) \underbrace{\int_1^\infty r'' \left(r''^2 - 1\right)^k \exp(-r''^2 R_d^2/(2\sigma^2)) \mathrm{d}r''}_{\mathcal{F}_k}. \tag{A4}$$

Applying integration by parts to $\mathcal{F}_k$ leads to the following recursion:

$$\mathcal{F}_k = \frac{2k\sigma^2}{R_d^2} \mathcal{F}_{k-1}, \tag{A5}$$

whose solution is $k!(2\sigma^2/R_d^2)^k \mathcal{F}_0$, where

$$\mathcal{F}_0 = \int_1^\infty r'' \exp(-r''^2 R_d^2/(2\sigma^2)) \mathrm{d}r'' = \frac{\sigma^2}{R_d^2} \exp(-R_d^2/(2\sigma^2)). \tag{A6}$$

Inserting the solution of $\mathcal{F}_k$ into (A4) and then into (A2) gives

$$
\int_0^{R_d} r' \exp(-r'^2/(2\sigma^2)) \mathrm{I}_0 \left(\frac{rr'}{\sigma^2} \right) \mathrm{d}r'
$$

$$
= \sigma^2 \exp(r^2/(2\sigma^2)) - \sigma^2 \exp(-R_d^2/(2\sigma^2)) \sum_{k \geq 0} \left(\frac{r}{R_d} \right)^k \mathrm{I}_k \left(\frac{rR_d}{\sigma^2} \right). \quad \text{(A7)}
$$

Moreover, we can relate the generating function in (A7) to the Marcum Q-function $Q_M(a, b)$ through (Proakis 1983, p. 44; 2-1-123)

$$
\sum_{k \geq 0} \left(\frac{r}{R_d} \right)^k \mathrm{I}_k \left(\frac{rR_d}{\sigma^2} \right) = \exp(r^2/(2\sigma^2)) \exp(R_d^2/(2\sigma^2)) Q_1(r/\sigma, R_d/\sigma), \quad \text{(A8)}
$$

and hence

$$
\int_0^{R_d} r' \exp(-r'^2/(2\sigma^2)) \mathrm{I}_0 \left(\frac{rr'}{\sigma^2} \right) \mathrm{d}r' = \sigma^2 \exp(r^2/(2\sigma^2))(1 - Q_1(r/\sigma, R_d/\sigma)). \quad \text{(A9)}
$$

The Marcum Q-function is found in some, but not all, mathematical toolboxes, and hence (A7) can still be useful. Also, (A7) can be used to examine the limiting behaviour of the shaping function $\mathcal{S}$ defined in (2.2) as follows. Close to the wake source, the characteristic length σ is small, making the argument of the modified Bessel function sufficiently large to use the approximation (Abramowitz & Stegun 1972, p. 377; 9.7.1)

$$
\mathrm{I}_k \left(\frac{rR_d}{\sigma^2} \right) \sim \sigma \frac{\exp(rR_d/\sigma^2)}{\sqrt{2\pi r R_d}} \left(1 + O(\sigma^2) \right). \quad \text{(A10)}
$$

Using this approximation along with (A7) and $\lim_{\sigma \to 0} \sigma \exp(-c/\sigma^2) = 0$, we can approximate $\mathcal{S}$ for a small σ as

$$
\mathcal{S}|_{\sigma \ll} \approx \exp(r^2/(2\sigma^2)). \quad \text{(A11)}
$$

A similar result can be obtained from (A9) using the fact that the first-order Marcum Q-function $Q_1(a, b)$ vanishes for large values of b, which occurs when σ is small as $b = R_d/\sigma$.

Appendix B. Conservation of linear momentum

In this appendix, we present a derivation for the streamwise scaling function $C(x)$ to ensure that the wake form introduced in (2.2) conserves linear momentum. From the integral form of the conservation of linear momentum in the wake of a turbine, we have (Tennekes & Lumley 1972)

$$
2\pi\rho \int_0^{\infty} u(u_\infty - u) r \, \mathrm{d}r = \frac{1}{2} \rho C_t \pi R^2 u_\infty^2, \quad \text{(B1)}
$$

where ρ is the air density, C_t is the thrust coefficient, R is the turbine's radius, u_∞ is the free-stream wind speed, u is the wind speed in the turbine's wake and r is a radial

coordinate. By making use of the definition $W = 1 - u/u_\infty$, (B1) becomes

$$\underbrace{\int_0^\infty rW \, \mathrm{d}r}_{A_1} - \underbrace{\int_0^\infty rW^2 \, \mathrm{d}r}_{A_2} = R^2 C_t/4. \tag{B2}$$

From (2.2), the normalised wind-speed deficit W is

$$W = C \exp(-r^2/(2\sigma^2)) \frac{1}{\sigma^2} \int_0^{R_d} r' \exp(-r'^2/(2\sigma^2)) \mathrm{I}_0 \left(\frac{rr'}{\sigma^2} \right) \mathrm{d}r', \tag{B3}$$

and the corresponding integrals A_1 and A_2 are evaluated as follows.

B.1. *The integral A_1*

The integral A_1 is

$$A_1 = \frac{C}{\sigma^2} \int_0^\infty r \exp(-r^2/(2\sigma^2)) \left(\int_0^{R_d} r' \exp(-r'^2/(2\sigma^2)) \mathrm{I}_0 \left(\frac{rr'}{\sigma^2} \right) \mathrm{d}r' \right) \mathrm{d}r, \tag{B4}$$

which can be re-arranged as

$$A_1 = \frac{C}{\sigma^2} \int_0^{R_d} r' \exp(-r'^2/(2\sigma^2)) \left(\int_0^\infty r \exp(-r^2/(2\sigma^2)) \mathrm{I}_0 \left(\frac{rr'}{\sigma^2} \right) \mathrm{d}r \right) \mathrm{d}r'. \tag{B5}$$

The improper integral in (B5) is given by (A1), and hence,

$$A_1 = C \int_0^{R_d} r' \, \mathrm{d}r' = \frac{1}{2} R_d^2 C. \tag{B6}$$

B.2. *The integral A_2*

As for the integral A_2

$$A_2 = \frac{C^2}{\sigma^4} \int_0^\infty r \exp(-r^2/\sigma^2)$$
$$\times \left(\int_0^{R_d} \eta_1 \exp(-\eta_1^2/(2\sigma^2)) \mathrm{I}_0 \left(\frac{r\eta_1}{\sigma^2} \right) \mathrm{d}\eta_1 \int_0^{R_d} \eta_2 \exp(-\eta_2^2/(2\sigma^2)) \mathrm{I}_0 \left(\frac{r\eta_2}{\sigma^2} \right) \mathrm{d}\eta_2 \right) \mathrm{d}r. \tag{B7}$$

The dummy variable r' in (2.2) was replaced with the dummy variables η_1 and η_2 for each instance of this integral in W^2. We could not obtain a mathematically exact solution of A_2. However, we will present two approaches to obtain an approximate expression for A_2.

B.2.1. *Approach 1*

By re-arranging (B7), we get

$$A_2 = \frac{C^2}{\sigma^4} \int_0^{R_d} \int_0^{R_d} \eta_1 \eta_2 \exp\left(-\left(\eta_1^2 + \eta_2^2\right)/(2\sigma^2)\right)$$

$$\times \left(\int_0^\infty r \exp(-r^2/\sigma^2) \mathrm{I}_0\left(\frac{r\eta_1}{\sigma^2}\right) \mathrm{I}_0\left(\frac{r\eta_2}{\sigma^2}\right) \mathrm{d}r\right) \mathrm{d}\eta_1 \, \mathrm{d}\eta_2. \quad \text{(B8)}$$

The solution of the improper integral in (B8) is (Gradshteyn & Ryzhik 2007, p. 707; 6.633-4)

$$\int_0^\infty r \exp(-r^2/\sigma^2) \mathrm{I}_0\left(\frac{r\eta_1}{\sigma^2}\right) \mathrm{I}_0\left(\frac{r\eta_2}{\sigma^2}\right) \mathrm{d}r = \frac{1}{2}\sigma^2 \exp\left(\left(\eta_1^2 + \eta_2^2\right)/(4\sigma^2)\right) \mathrm{I}_0\left(\frac{\eta_1\eta_2}{2\sigma^2}\right), \quad \text{(B9)}$$

and hence (B8) simplifies to

$$A_2 = \frac{R_d^2 C^2}{2\tilde{\sigma}^2} \int_0^1 \int_0^1 \xi_1 \xi_2 \exp\left(-\left(\xi_1^2 + \xi_2^2\right)/(4\tilde{\sigma}^2)\right) \mathrm{I}_0\left(\frac{\xi_1\xi_2}{2\tilde{\sigma}^2}\right) \mathrm{d}\xi_1 \, \mathrm{d}\xi_2, \quad \text{(B10)}$$

where $\xi_1 = \eta_1/R_d$, $\xi_2 = \eta_2/R_d$ and $\tilde{\sigma} = \sigma/R_d$. Equation (B10) contains an integral over a unit square in the first quadrant of the $\xi_1 - \xi_2$ space. We can split this integral into A_2', which is the integral over the quarter of the unit circle inscribed in the unit square of integration, and A_2'', which is the integral over the left-over area (i.e. $A_2 = A_2' + A_2''$). By introducing the polar coordinates $r_\xi - \theta_\xi$ that satisfy $\xi_1 = r_\xi \cos\theta_\xi$ and $\xi_2 = r_\xi \sin\theta_\xi$, the integral A_2' becomes

$$A_2' = \frac{R_d^2 C^2}{4\tilde{\sigma}^2} \int_0^1 r_\xi^3 \exp(-r_\xi^2/(4\tilde{\sigma}^2)) \int_0^{\pi/2} \sin(2\theta_\xi) \mathrm{I}_0\left(\frac{r_\xi^2 \sin(2\theta_\xi)}{4\tilde{\sigma}^2}\right) \mathrm{d}\theta_\xi \, \mathrm{d}r_\xi. \quad \text{(B11)}$$

The solution to inner integral in (B11) (over θ_ξ) is $4\tilde{\sigma}^2 r_\xi^{-2} \sinh(0.25 \, r_\xi^2 \tilde{\sigma}^{-2})$ (Gradshteyn & Ryzhik 2007, p. 725; 6.681-8), and hence

$$A_2' = R_d^2 C^2 \int_0^1 r_\xi \exp(-r_\xi^2/(4\tilde{\sigma}^2)) \sinh\left(\frac{r_\xi^2}{4\tilde{\sigma}^2}\right) \mathrm{d}r_\xi$$

$$= \frac{R_d^2 C^2}{4}\left(1 - \frac{2\sigma^2}{R_d^2}\left(1 - \exp(-R_d^2/(2\sigma^2))\right)\right). \quad \text{(B12)}$$

As for the integral A_2'', we have

$$A_2'' = \frac{R_d^2 C^2}{4\tilde{\sigma}^2} \int_0^{\pi/2} \sin(2\theta_\xi) \int_1^{\sec\theta_\xi} r_\xi^3 \exp(-r_\xi^2/(4\tilde{\sigma}^2)) \mathrm{I}_0\left(\frac{r_\xi^2 \sin(2\theta_\xi)}{4\tilde{\sigma}^2}\right) \mathrm{d}r_\xi \, \mathrm{d}\theta_\xi. \quad \text{(B13)}$$

The integral over r_ξ in (B13) is not straightforward to solve analytically. However, using numerical evaluation of the integral A_2 (B7) and (B12), we can show that

$$A_2'' \approx \frac{R_d^2 C^2}{8}\left(1 - \frac{\sigma^2}{R_d^2}\left(1 - \exp(-R_d^2/\sigma^2)\right)\right)$$

$$+ \frac{R_d^2 C^2}{10}\left(1 - \frac{23\sigma^2}{R_d^2}\left(1 - \exp(-R_d^2/(22\sigma^2))\right)\right), \quad \text{(B14)}$$

and hence $A_2 \approx R_d^2 C^2 \lambda/4$, where

$$\lambda = 1.9 - \frac{2\sigma^2}{R_d^2}\left(1 - \exp(-R_d^2/(2\sigma^2))\right) - \frac{\sigma^2}{2R_d^2}\left(1 - \exp(-R_d^2/\sigma^2)\right)$$
$$- \frac{46\sigma^2}{5R_d^2}\left(1 - \exp(-R_d^2/(22\sigma^2))\right). \tag{B15}$$

B.2.2. *Approach 2*

The difficulty in solving the integral A_2 in (B7) analytically arises in part due to the presence of the modified Bessel function I_0, which emerges from the integration of a Gaussian function over a circular disk. Geometrically, the integral A_2 represents the volume between the surface $W^2(y, z)$ and the y–z plane (scaled by 2π for the azimuthal integration over θ). This volume is an integral quantity and hence is not exclusive to a specific shape of the disk source, but can be obtained from other shapes by appropriate sizing and scaling relative to the circular disk source. Unlike the circular case, the equations for a rectangular disk source can be solved exactly. Given that we are considering an axisymmetric wake, modelled through the diffusion of a passive scalar from a uniform circular disk source, we seek an approximate solution for the integral A_2 by using a uniform square disk source with a side length $2l$. This approximation is intended solely for solving A_2 and is not related to the presented wake model which assumes a circular disk source. We define $\tilde{W}$ as the normalised wind-speed deficit due to a square disk source, and seek to evaluate $\tilde{A}_2$ such that

$$\tilde{A}_2 = \int_{-\infty}^{\infty} \int_{-\infty}^{\infty} \tilde{W}^2 \, \mathrm{d}y \, \mathrm{d}z. \tag{B16}$$

For a square disk source, $\tilde{W}$ can be expressed in terms of the error function (erf) as (Ng & Geller 1969; Crank 1979)

$$\tilde{W} = \frac{\pi C}{2}\left[\mathrm{erf}\left(\frac{l - y}{\sqrt{2}\sigma}\right) + \mathrm{erf}\left(\frac{l + y}{\sqrt{2}\sigma}\right)\right]\left[\mathrm{erf}\left(\frac{l - z}{\sqrt{2}\sigma}\right) + \mathrm{erf}\left(\frac{l + z}{\sqrt{2}\sigma}\right)\right]. \tag{B17}$$

Since C and σ are functions of the streamwise direction x but are not functions of y and z, they are the assumed to be same for the circular and square disk sources. Because y and z are separable in (B17), we can consider only one of them in the integration over the y–z plane (B16), and the other integral would be the same. For the y direction, the integral in (B16) yields an integration in the form

$$\mathcal{M}(a) = \sqrt{2}\sigma \int_{-\infty}^{\infty} (\mathrm{erf}\,(a - \eta) + \mathrm{erf}\,(a + \eta))^2 \, \mathrm{d}\eta, \tag{B18}$$

where $a = l/(\sqrt{2}\sigma)$, and $\eta = y/(\sqrt{2}\sigma)$. According to Ali *et al.* (2024c),

$$\int_{-\infty}^{\infty} (\mathrm{erf}(a - \eta) + \mathrm{erf}(a + \eta))^2 \, \mathrm{d}\eta = 8\left(a\,\mathrm{erf}(\sqrt{2}a) + \frac{\exp(-2a^2) - 1}{\sqrt{2\pi}}\right), \tag{B19}$$

and hence

$$\tilde{A}_2 = 16\pi C^2 l^2 \left(\sqrt{\pi}\,\mathrm{erf}\left(\frac{l}{\sigma}\right) - \frac{\sigma}{l}\left(1 - \exp(-l^2/\sigma^2)\right)\right)^2. \tag{B20}$$

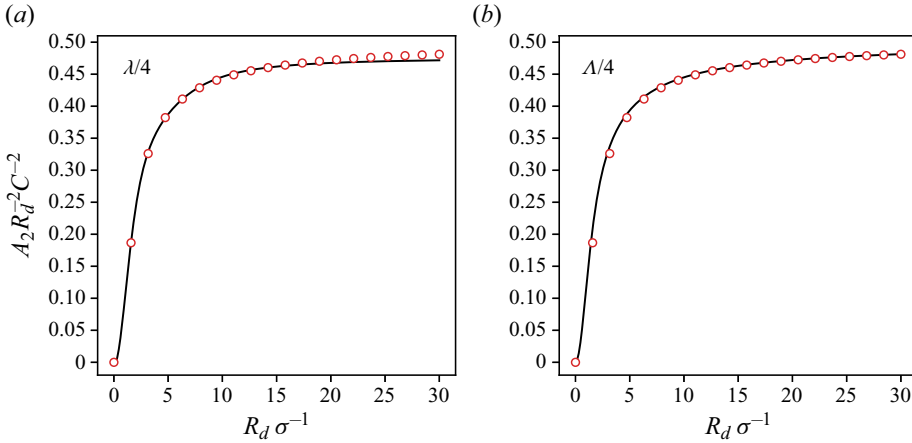Figure 7. A comparison between (*a*) the function λ (B15) and (*b*) the function Λ (B21) against the numerical evaluation of A_2 (B7) shown by the red markers.

Through a comparison with numerical evaluation of A_2 (B7) and exploiting the form in (B20) assuming that $l = R_d$, we can show that $A_2 \approx R_d^2 C^2 \Lambda / 4$, where

$$\Lambda = 2 \left(\mathrm{erf}\left(\frac{R_d}{\sigma} \right) - \frac{\sigma}{\sqrt{\pi} R_d} \left(1 - \exp(-R_d^2/\sigma^2) \right) \right)^2. \tag{B21}$$

B.3. *An expression for the scaling function C*

Figure 7 shows a comparison between the approximate solutions of the integral A_2: λ (B15) and Λ (B21) against numerical evaluation of A_2. From this comparison, we adopt the Λ function as an approximate solution to A_2. Having evaluated the integrals A_1 (B6) and A_2 (B21), the conservation of linear momentum (B2) simplifies to $\Lambda C^2 - 2C + (R/R_d)^2 C_t = 0$, whose solution is

$$C \approx \frac{1 - \sqrt{1 - (R/R_d)^2 \Lambda C_t}}{\Lambda}. \tag{B22}$$

We use the approximation symbol in (B22) because the integral A_2 is not mathematically exact in the sense that we could not derive (B21) directly from the main expression of A_2 (B7), but from an alias of A_2 (B16).

Appendix C. Review of analytical wake models

In this appendix we review some engineering wake models from the literature that are included in the comparisons of § 3. We mainly focus on the Gaussian model of Bastankhah & Porté-Agel (2014) and the super-Gaussian models of Blondel & Cathelain (2020), Cathelain *et al.* (2020) and Blondel (2023).

C.1. *Gaussian wake*

In the Gaussian model of Bastankhah & Porté-Agel (2014), the normalised wind-speed deficit W_g (the subscript g means Gaussian) is expressed as

$$W_g = C_g(x) \exp(-r^2/(2\sigma_g^2)), \tag{C1}$$

where the scaling function $C_g(x)$ is

$$C_g(x) = 1 - \sqrt{1 - \frac{C_t}{8\left(\sigma_g/D\right)^2}}, \tag{C2}$$

and the length scale σ_g expands linearly in the streamwise direction following

$$\sigma_g = k_g^* x + \varepsilon_g D. \tag{C3}$$

The rate of wake expansion k_g^* is assumed to linearly depend on the free-stream turbulence intensity T_i

$$k_g^* = 0.003678 + 0.3837\, T_i, \tag{C4}$$

and the initial wake width ε_g is

$$\varepsilon_g = 0.2\sqrt{\beta}, \tag{C5}$$

where

$$\beta = \frac{1 + \sqrt{1 - C_t}}{2\sqrt{1 - C_t}}. \tag{C6}$$

C.2. *Super-Gaussian wake*

In a super-Gaussian model, the normalised wind-speed deficit W_{sg} (the subscript *sg* means super-Gaussian) is

$$W_{sg} = C_{sg}(x)\exp(-r^n/(2\sigma_{sg}^2)), \tag{C7}$$

where n is a super-Gaussian exponent, C_{sg} is a super-Gaussian scaling function and σ_{sg} is a characteristic length scale of the super-Gaussian model. Note that n, C_{sg} and σ_{sg} will have the same formulation for all the considered super-Gaussian models, and hence were not given special subscripts although their tuneable parameters will have different values, as will be discussed. Blondel & Cathelain (2020) derived an expression for $C_{sg}(x)$ based on the conservation of linear momentum to be

$$C_{sg}(x) = 2^{-1+2/n} - \sqrt{2^{-2+4/n} - \frac{nC_t}{16\Gamma(2/n)\,(\sigma_{sg}/D)^{4/n}}}, \tag{C8}$$

where Γ is the gamma function. The super-Gaussian exponent n takes the form

$$n = a_f \exp(b_f x) + c_f, \tag{C9}$$

where a_f, b_f and c_f are tuneable parameters. The characteristic length scale σ_{sg} is

$$\sigma_{sg} = (a_s T_i + b_s)\, x + c_s\sqrt{\beta}D, \tag{C10}$$

where a_s, b_s and c_s are tuneable parameters, and β is given by (C6). The six tuneable parameters a_f, b_f, c_f, a_s, b_s and c_s are obtained from fitting LES data differently for each of the considered super-Gaussian models, as summarised in table 1. In the model of Blondel & Cathelain (2020), all six parameters have numeric values as listed in the first row of table 1. However, in the model of Cathelain *et al.* (2020), the parameters b_f and c_s are defined to be functions of T_i and C_t, respectively,

$$(b_f)_{C20} = 1.59\exp(-23.31\, T_i) - 2.15 \tag{C11}$$

$$(c_s)_{C20} = 0.0564\, C_t + 0.13. \tag{C12}$$

Model	a_f	b_f	c_f	a_s	b_s	c_s
Blondel & Cathelain (2020)	3.11	-0.68	2.41	0.17	0.005	0.2
Cathelain *et al.* (2020)	$C_{sg}(0) = a$	(C11)	2.98	0.18	0.0119	(C12)
Blondel (2023)	(C13)	(C14)	2.0	0.28	0.01	(C15)

Table 1. The numerical values of the tuneable parameters in (C9) and (C10) for different super-Gaussian models.
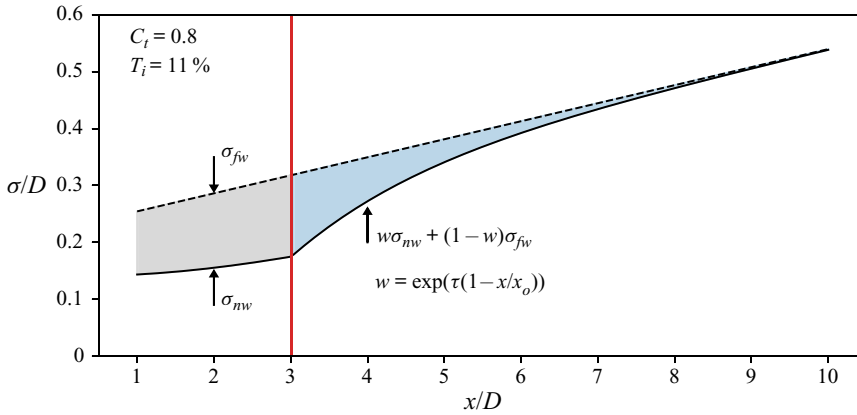

Figure 8. The streamwise evolution of the length scale σ (solid black curve) for $C_t = 0.8$ and $T_i = 11\,\%$. The range of the near wake x_o (2.14) is shown by a vertical red line. The far-wake length scale σ_{fw} (2.12) is shown by a dashed line. The difference between σ_{fw} and the adopted expression for σ (2.16) is shaded in grey for the near-wake region and in blue for the far-wake region. The parameter $\tau = 2$ as outlined in § 2.4.

Also, a_f is obtained from one-dimensional momentum theory (Burton *et al.* 2021) using root finding to ensure that the maximum deficit at the start of the wake equals the axial induction of the turbine $a = 0.5(1 - \sqrt{1 - C_t})$. In the model of Blondel (2023), the parameters a_f, b_f and c_s are defined as

$$(a_f)_{B23} = -8.2635\,C_t^3 + 8.5939\,C_t^2 - 8.9691\,C_t + 10.7286 \tag{C13}$$

$$(b_f)_{B23} = 1.68 \exp(-25.98\,T_i) - 1.06 \tag{C14}$$

$$(c_s)_{B23} = 0.1\,C_t + 0.1. \tag{C15}$$

Appendix D. Supplementary material

In this appendix we include some supplementary figures to the main text. Figure 8 shows the streamwise profile of the adopted length scale σ (2.16) and the far-wake length scale σ_{fw} (2.12) for an exemplary case of $C_t = 0.8$ and $T_i = 11\,\%$. The near-wake adjustment due to the definition of σ_{nw} (2.15) is indicated by the grey-shaded region, whereas the role of the exponential blend between σ_{nw} and σ_{fw} (2.16) in the far wake is indicated by the blue-shaded region. The length scale σ approaches σ_{fw} in the very-far wake where both the proposed wake model (2.2) and the super-Gaussian model (Cathelain *et al.* 2020, for which σ_{fw} in (2.12) is designed) approach a Gaussian wake profile.
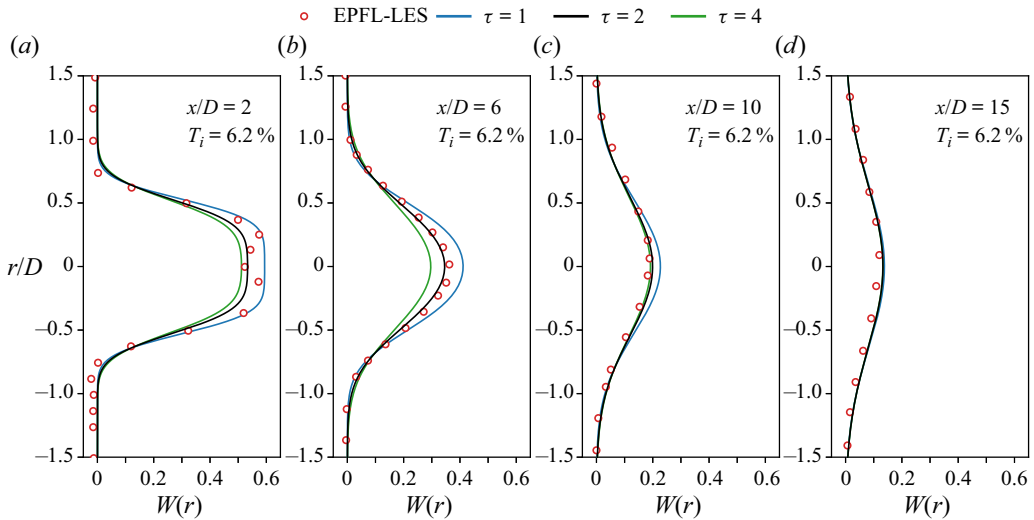
Figure 9. Sensitivity of the proposed wake model to the parameter τ in the expression for σ_{nw} (2.15) and in the exponential blend between σ_{nw} and σ_{fw} (2.16). Three values are tested: $\tau = 1$ (blue), $\tau = 2$ (black; original value in (2.15)) and $\tau = 4$ (green) against LES results (red). Shown is the fourth row ($T_i = 6.2\,\%$) of the LES deficit profiles indicated in figure 3.

The expression for the near-wake length scale σ_{nw} (2.15) is formed by the superposition of a contraction and an expansion tendencies. The parameter τ in the contraction term was obtained empirically using the LES deficit profiles of figure 3, as outlined in § 2.4. Figure 9 presents an exemplary sensitivity analysis of the parameter τ for the case of $T_i = 6.2\,\%$ (fourth row) of the LES deficit profiles in figure 3. Figure 9 indicates a slight variation in the deficit W for the three tested values of τ. When τ was halved from 2 to 1 (50\,\% drop), the increase in the deficit W was approximately 6\,\% of the free-stream wind speed u_∞ at $x/D = 2$, and approximately 6.6\,\% of u_∞ at $x/D = 6$. Moreover, when τ was doubled from 2 to 4 (a 100\,\% increase), the deficit W dropped by approximately 2\,\% of u_∞ at $x/D = 2$ and by approximately 5\,\% of u_∞ at $x/D = 6$. These variations occurred for the near-wake case ($x/D = 2$) and for $x/D = 6$ along the wake's centreline, but considering the full deficit profile normal to the streamwise direction $\tau = 2$ gives best agreement. The other cases show negligible differences.

REFERENCES

ABRAMOWITZ, M. & STEGUN, I.A. 1972 *Handbook of Mathematical Functions with Formulas, Graphs, and Mathematical Tables*. Dover.

ALI, K., SCHULTZ, D.M., REVELL, A., STALLARD, T. & OURO, P. 2023 Assessment of five wind-farm parameterizations in the weather research and forecasting model: a case study of wind farms in the North Sea. *Mon. Weath. Rev.* **151** (9), 2333–2359.

ALI, K., STALLARD, T. & OURO, P. 2024a Analytical evaluation of non-axisymmetric Gaussian wind-turbine wake including yaw and wind-veer effects [Computer software]. https://doi.org/10.5281/zenodo.12784758.

ALI, K., STALLARD, T. & OURO, P. 2024b Evaluating wind-farm power generation using a new direct integration of axisymmetric turbine wake. *J. Phys.: Conf. Ser.* **2767** (9), 092015.

ALI, K., STALLARD, T. & OURO, P. 2024c An exact solution of a momentum-conservation condition for scalar diffusion from a uniform-concentration region. Preprint https://doi.org/10.13140/RG.2.2.27966.09287.

AUBRUN, S., LOYER, S., HANCOCK, P.E. & HAYDEN, P. 2013 Wind turbine wake properties: comparison between a non-rotating simplified wind turbine model and a rotating model. *J. Wind Engng Ind. Aerodyn.* **120**, 1–8.

BALAKRISHNAN, R.K. & HUR, S.-H. 2022 Maximization of the power production of an offshore wind farm. *Appl. Sci.* **12** (8), 4013.

BASTANKHAH, M. & PORTÉ-AGEL, F. 2014 A new analytical model for wind-turbine wakes. *Renew. Energy* **70**, 116–123.

BASTANKHAH, M. & PORTÉ-AGEL, F. 2016 Experimental and theoretical study of wind turbine wakes in yawed conditions. *J. Fluid Mech.* **806**, 506–541.

BASTANKHAH, M. & PORTÉ-AGEL, F. 2017 Wind tunnel study of the wind turbine interaction with a boundary-layer flow: upwind region, turbine performance, and wake region. *Phys. Fluids* **29** (6), 065105.

BASTANKHAH, M., WELCH, B.L., MARTÍNEZ-TOSSAS, L.A., KING, J. & FLEMING, P. 2021 Analytical solution for the cumulative wake of wind turbines in wind farms. *J. Fluid Mech.* **911**, A53.

BAY, C.J., ANNONI, J., TAYLOR, T., PAO, L. & JOHNSON, K. 2018 Active power control for wind farms using distributed model predictive control and nearest neighbor communication. In *2018 Annual American Control Conference (ACC)*, pp. 682–687. IEEE.

BLONDEL, F. 2023 Brief communication: a momentum-conserving superposition method applied to the super-Gaussian wind turbine wake model. *Wind Energy Sci.* **8** (2), 141–147.

BLONDEL, F. & CATHELAIN, M. 2020 An alternative form of the super-Gaussian wind turbine wake model. *Wind Energy Sci.* **5** (3), 1225–1236.

BUHL, M.L. 2005 A new empirical relationship between thrust coefficient and induction factor for the turbulent windmill state. *Tech. Rep.* NREL/TP-500-36834. National Renewable Energy Laboratory, Golden, CO.

BURTON, T., SHARPE, D., JENKINS, N. & BOSSANYI, E. 2021 *Wind Energy Handbook*, 3rd edn. John Wiley & Sons.

CARBAJO FUERTES, F., MARKFORT, C.D. & PORTÉ-AGEL, F. 2018 Wind turbine wake characterization with nacelle-mounted wind lidars for analytical wake model validation. *Remote Sens.* **10** (5), 668.

CATHELAIN, M., BLONDEL, F., JOULIN, P.A. & BOZONNET, P. 2020 Calibration of a super-Gaussian wake model with a focus on near-wake characteristics. *J. Phys.: Conf. Ser.* **1618** (6), 062008.

CHENG, W.-C. & PORTÉ-AGEL, F. 2018 A simple physically-based model for wind-turbine wake growth in a turbulent boundary layer. *Boundary-Layer Meteorol.* **169** (1), 1–10.

CRANK, J. 1979 *The Mathematics of Diffusion*. Oxford University Press.

CRESPO, A. & HERNANDEZ, J. 1996 Turbulence characteristics in wind-turbine wakes. *J. Wind Engng Ind. Aerodyn.* **61** (1), 71–85.

DAI, L., LUO, Z., GUO, T., CHAO, H., DONG, G. & HU, Z. 2024 Two three-dimensional super-Gaussian wake models for hilly terrain. *J. Renew. Sustain. Energy* **16** (1), 013304.

FITCH, A.C., OLSON, J.B., LUNDQUIST, J.K., DUDHIA, J., GUPTA, A.K., MICHALAKES, J. & BARSTAD, I. 2012 Local and mesoscale impacts of wind farms as parameterized in a mesoscale NWP model. *Mon. Weath. Rev.* **140** (9), 3017–3038.

FREITAS, S., ROWEN, M., DIAZ, G.N. & ERBSLÖH, S. 2024 Ranking multi-fidelity model performances in reproducing internal and external wake impacts at neighbouring offshore wind farms. *J. Phys.: Conf. Ser.* **2767** (9), 092045.

GLAUERT, H. 1926 The analysis of experimental results in the windmill brake and vortex ring states of an airscrew. *ARC/R & M*-1026. H.M. Stationery Office.

GLOBAL WIND ENERGY COUNCIL 2024 Global wind report 2024. https://gwec.net/global-wind-report-2024/.

GÖÇMEN, T., VAN DER LAAN, P., RÉTHORÉ, P.-E., DIAZ, A.P., LARSEN, G.C. & OTT, S. 2016 Wind turbine wake models developed at the technical university of Denmark: a review. *Renew. Sustain. Energy Rev.* **60**, 752–769.

GRADSHTEYN, I.S. & RYZHIK, I.M. 2007 Table of integrals, series, and products. In *6-7 – Definite Integrals of Special Functions*, 7th edn. (ed. A. Jeffrey, D. Zwillinger, I.S. Gradshteyn & I.M. Ryzhik), pp. 631–857. Academic.

HANNA, S.R. 1981 Lagrangian and Eulerian time-scale relations in the daytime boundary layer. *J. Appl. Meteorol. Climatol.* **20** (3), 242–249.

HAY, J.S. & PASQUILL, F. 1959 Diffusion from a continuous source in relation to the spectrum and scale of turbulence. *Adv. Geophys.* **6**, 345–365.

HOU, P., HU, W., CHEN, C., SOLTANI, M. & CHEN, Z. 2016 Optimization of offshore wind farm layout in restricted zones. *Energy* **113**, 487–496.

HOWLAND, M.F., GHATE, A.S., LELE, S.K. & DABIRI, J.O. 2020 Optimal closed-loop wake steering – part 1: conventionally neutral atmospheric boundary layer conditions. *Wind Energy Sci.* **5** (4), 1315–1338.

ISHIHARA, T. & QIAN, G.-W. 2018 A new Gaussian-based analytical wake model for wind turbines considering ambient turbulence intensities and thrust coefficient effects. *J. Wind Engng Ind. Aerodyn.* **177**, 275–292.

IVANELL, S., MIKKELSEN, R., SØRENSEN, J.N. & HENNINGSON, D. 2010 Stability analysis of the tip vortices of a wind turbine. *Wind Energy* **13** (8), 705–715.

JENSEN, N.O. 1983 A note on wind generator interaction. *Risø-M* 2411. Risø National Laboratory.

KEANE, A., AGUIRRE, P.E.O., FERCHLAND, H., CLIVE, P. & GALLACHER, D. 2016 An analytical model for a full wind turbine wake. *J. Phys.: Conf. Ser.* **753** (3), 032039.

KRUTOVA, M., PASKYABI, M.B., NIELSEN, F.G. & REUDER, J. 2020 Evaluation of Gaussian wake models under different atmospheric stability conditions: comparison with large eddy simulation results. *J. Phys.: Conf. Ser.* **1669** (1), 012016.

VAN DER LAAN, M.P., GARCÍA-SANTIAGO, O., SØRENSEN, N., TROLDBORG, N., RISCO, J. & BADGER, J. 2023 Simulating wake losses of the Danish Energy Island wind farm cluster. *J. Phys.: Conf. Ser.* **2505**, 012015.

LARSEN, G.C. 1988 A simple wake calculation procedure. *Risø-M* 2760. Risø National Laboratory, Denmark.

LEE, J.H.-W. & CHU, V.H. 2003 *Turbulent Jets and Plumes: A Lagrangian Approach*. Springer.

LIEW, J., HECK, K.S. & HOWLAND, M.F. 2024 Unified momentum model for rotor aerodynamics across operating regimes. *Nat. Commun.* **15** (1), 6658.

MAAS, O. & RAASCH, S. 2022 Wake properties and power output of very large wind farms for different meteorological conditions and turbine spacings: a large-eddy simulation case study for the German Bight. *Wind Energy Sci.* **7** (2), 715–739.

NARASIMHAN, G., GAYME, D.F. & MENEVEAU, C. 2024 Analytical wake modeling in atmospheric boundary layers: accounting for wind veer and thermal stratification. *J. Phys.: Conf. Ser.* **2767** (9), 092018.

NG, E.W. & GELLER, M. 1969 A table of integrals of the error functions. *J. Res. Natl Bur. Stand.* **73B**.

NIAYIFAR, A. & PORTÉ-AGEL, F. 2015 A new analytical model for wind farm power prediction. *J. Phys.: Conf. Ser.* **625** (1), 012039.

OURO, P. & LAZENNEC, M. 2021 Theoretical modelling of the three-dimensional wake of vertical axis turbines. *Flow* **1**, E3.

PEDERSEN, J.G., SVENSSON, E., POULSEN, L. & NYGAARD, N.G. 2022 Turbulence optimized park model with Gaussian wake profile. *J. Phys.: Conf. Ser.* **2265** (2), 022063.

PORTÉ-AGEL, F., BASTANKHAH, M. & SHAMSODDIN, S. 2020 Wind-turbine and wind-farm flows: a review. *Boundary-Layer Meteorol.* **174** (1), 1–59.

POSA, A. & BROGLIA, R. 2021 Momentum recovery downstream of an axial-flow hydrokinetic turbine. *Renew. Energy* **170**, 1275–1291.

PROAKIS, J. 1983 *Digital Communications*. McGraw-Hill.

ROSENHEINRICH, W. 2017 *Tables of Some Indefinite Integral of Bessel Functions of Integer Order*. Ernst - Abbe - Hochschule Jena.

SCHREIBER, J., BALBAA, A. & BOTTASSO, C.L. 2020 Brief communication: a double-Gaussian wake model. *Wind Energy Sci.* **5** (1), 237–244.

SHAPIRO, C.R., STARKE, G.M. & GAYME, D.F. 2022 Turbulence and control of wind farms. *Annu. Rev. Control Rob. Auton. Syst.* **5**, 579–602.

SHAPIRO, C.R., STARKE, G.M., MENEVEAU, C. & GAYME, D.F. 2019 A wake modeling paradigm for wind farm design and control. *Energies* **12** (15), 2956.

SØRENSEN, J.N., MIKKELSEN, R., SARMAST, S., IVANELL, S. & HENNINGSON, D. 2014 Determination of wind turbine near-wake length based on stability analysis. *J. Phys.: Conf. Ser.* **524** (1), 012155.

SØRENSEN, J.N., MIKKELSEN, R.F., HENNINGSON, D.S., IVANELL, S., SARMAST, S. & ANDERSEN, S.J. 2015 Simulation of wind turbine wakes using the actuator line technique. *Phil. Trans. R. Soc. Lond.* A **373** (2035), 20140071.

TABIB, M., RASHEED, A. & KVAMSDAL, T. 2015 LES and RANS simulation of onshore Bessaker wind farm: analysing terrain and wake effects on wind farm performance. *J. Phys.: Conf. Ser.* **625**, 012032.

TAYLOR, G.I. 1921 Diffusion by continuous movements. *Proc. Lond. Math. Soc.* **20**, 196–212.

TENNEKES, H. & LUMLEY, J.L. 1972 *A First Course in Turbulence*. MIT.

TROLDBORG, N., SORENSEN, J.N. & MIKKELSEN, R. 2010 Numerical simulations of wake characteristics of a wind turbine in uniform inflow. *Wind Energy* **13** (1), 86–99.

VAHIDI, D. & PORTÉ-AGEL, F. 2022 A physics-based model for wind turbine wake expansion in the atmospheric boundary layer. *J. Fluid Mech.* **943**, A49.

VERMEULEN, P.J. 1980 An experimental analysis of wind turbine wakes. In *Proceedings of the International Symposium on Wind Energy Systems, Cambridge, UK, September 8–11*, pp. 431–450. Cambridge University Press.

VOUTSINAS, S., RADOS, K. & ZERVOS, A. 1990 On the analysis of wake effects in wind parks. *Wind Engng* **14** (4), 204–219.

WANG, J., FOLEY, S., NANOS, E.M., YU, T., CAMPAGNOLO, F., BOTTASSO, C.L., ZANOTTI, A. & CROCE, A. 2017 Numerical and experimental study of wake redirection techniques in a boundary layer wind tunnel. *J. Phys.: Conf. Ser.* **854** (1), 012048.

ZHAN, L., LETIZIA, S. & IUNGO, G.V. 2020 Optimal tuning of engineering wake models through lidar measurements. *Wind Energy Sci.* **5** (4), 1601–1622.

ZHANG, S., GAO, X., MA, W., LU, H., LV, T., XU, S., ZHU, X., SUN, H. & WANG, Y. 2023 Derivation and verification of three-dimensional wake model of multiple wind turbines based on super-Gaussian function. *Renew. Energy* **215**, 118968.